nature genetics

Article

https://doi.org/10.1038/s41588-024-01902-8

Antagonism between H3K27me3 and genome–lamina association drives atypical spatial genome organization in the totipotent embryo

Received: 17 January 2023

Accepted: 8 August 2024

Published online: 16 September 2024

Check for updates

Isabel Guerreiro[1,2,6] ✉, Franka J. Rang[1,2,6], Yumiko K. Kawamura[3], Carla Kroon-Veenboer[1,2], Jeroen Korving[1,2], Femke C. Groenveld[1,2,4], Ramada E. van Beek[1,2], Silke J. A. Lochs[1,2], Ellen Boele[1,2], Antoine H. M. F. Peters[3,5] & Jop Kind[1,2,4] ✉

In mammals, early embryonic development exhibits highly unusual spatial positioning of genomic regions at the nuclear lamina, but the mechanisms underpinning this atypical genome organization remain elusive. Here, we generated single-cell profiles of lamina-associated domains (LADs) coupled with transcriptomics, which revealed a striking overlap between preimplantation-specific LAD dissociation and noncanonical broad domains of H3K27me3. Loss of H3K27me3 resulted in a restoration of canonical LAD profiles, suggesting an antagonistic relationship between lamina association and H3K27me3. Tethering of H3K27me3 to the nuclear periphery showed that the resultant relocalization is partially dependent on the underlying DNA sequence. Collectively, our results suggest that the atypical organization of LADs in early developmental stages is the result of a tug-of-war between intrinsic affinity for the nuclear lamina and H3K27me3, constrained by the available space at the nuclear periphery. This study provides detailed insight into the molecular mechanisms regulating nuclear organization during early mammalian development.

Mammalian development begins with the fusion of two differentiated cells, the gametes, which give rise to a totipotent zygote. The embryo subsequently undergoes multiple cycles of cell division, with inner cells progressively transitioning to a pluripotent state, whereas outer cells commit to the extra-embryonic lineage by the time of implantation in the uterus. These events are accompanied by extensive epigenetic reprogramming, as well as major changes in spatial genome organization (reviewed in refs. 1,2).

One important feature of nuclear organization is the localization of genomic regions at the nuclear lamina (NL). These genomic regions, termed LADs, are characterized by low gene density, low gene expression, high repeat content and other features of constitutive heterochromatin. Moreover, LADs have been shown to play an important role in genome architecture and gene expression in various systems (reviewed in refs. 3–5). LADs are typically detected using DNA adenine methyltransferase identification (DamID)[6], which is based on the expression

[1]Hubrecht Institute, Royal Netherlands Academy of Arts and Sciences (KNAW) and University Medical Center Utrecht, Utrecht, the Netherlands. [2]Oncode Institute, Utrecht, the Netherlands. [3]Friedrich Miescher Institute for Biomedical Research (FMI), Basel, Switzerland. [4]Department of Molecular Biology, Radboud Institute for Molecular Life Sciences, Radboud University Nijmegen, Nijmegen, the Netherlands. [5]Faculty of Sciences, University of Basel, Basel, Switzerland. [6]These authors contributed equally: Isabel Guerreiro, Franka J. Rang. ✉e-mail: i.guerreiro@hubrecht.eu; j.kind@hubrecht.eu

of *Escherichia coli* DNA adenine methyltransferase (Dam) fused to a protein-of-interest and subsequent methylation in vivo. Fusing Dam to Lamin B1 results in the specific methylation of LADs, which can subsequently be sequenced and mapped to the genome.

Previous work mapping LADs in preimplantation development has shown atypical patterns of lamina association at these stages. Maternal LADs are established de novo following fertilization, whereas paternal LADs undergo massive rearrangements between the zygote and 2-cell stages. Consequently, maternal and paternal genomes show differences in lamina association up until the 8-cell stage[1].

In addition to LADs, other chromatin features undergo extensive rewiring during early stages of development[7–13]. Trimethylation of histone H3 at lysine 27 (H3K27me3), a histone post-translational modification associated with the repression of developmental genes, is deposited by Polycomb repressive complex (PRC) 2. After fertilization, H3K27me3 loses its typical distribution at promoters of developmental genes in both alleles while retaining noncanonical broad distal domains in regions devoid of developmental genes in the maternal allele[13]. Trimethylation of histone H3 at lysine 9 (H3K9me3), a mark found associated with LADs in several cell types[14], also shows an unusual distribution and allelic asymmetry in early mouse development. H3K9me3 extensively overlaps with H3K27me3 during early developmental stages across the genome, in contrast to what has been reported in other biological systems[11].

Although low-input technologies have recently shed light on the chromatin state and nuclear architecture of the early mouse embryo, the underlying mechanisms and interdependencies between different epigenetic layers remain largely unexplored. In addition, although cell-to-cell variability in gene expression and chromatin modifiers is proposed to contribute to early cell fate choices[15–17], the extent and role of variability in the genome–lamina association during preimplantation development is unknown. Here, we profile single-cell allele-resolved LADs throughout a range of early developmental stages to provide mechanistic insight into the atypical genome–NL associations that characterize the nucleus of the totipotent embryo.

Results

LADs vary extensively between single blastomeres

Our previous work in preimplantation development suggested that cell-to-cell variability in LADs is particularly high between single cells in early developmental stages[1]. To address this in greater detail, we have made use of single-cell DamID and transcription sequencing (scDam&T-seq)[18] to: (1) obtain superior signal-to-noise levels, (2) increase throughput, (3) register the embryo-of-origin for each cell and (4) combine DamID with transcriptomics in the same cell (Extended Data Fig. 1a,b).

We obtained a total of 755 single-cell LAD profiles from zygotes, 2-cell and 8-cell embryos, as well as mouse embryonic stem cells (mESCs) (Extended Data Fig. 1b,d and Supplementary Tables 1 and 2). Average LAD profiles per stage showed high concordance with previously published genomic and imaging-based data (Extended Data Fig. 1e,g), and transcriptional profiles displayed the expected patterns (Extended Data Fig. 1h).

For each cell, we obtained the LAD profile and the corresponding gene expression readout (Fig. 1a and Extended Data Fig. 2a). Similar to the transcriptional data, representation of the DamID data using uniform manifold approximation and projection (UMAP) shows clear per stage clustering (Fig. 1b,c), demonstrating that single-cell LAD profiles are stage-specific.

To understand whether there were differences in cell-to-cell LAD variability across stages, we converted single-cell genome–lamina values to an aggregate contact frequency (CF) values, which represents the fraction of cells in which a genomic bin is associated with the lamina[19]. CF distributions per stage indicated extensive LAD variability at the 2-cell and 8-cell stages (Extended Data Fig. 2a,b). Next, we calculated the similarity between single-cell LAD profiles (Methods), which showed that 2-cell genome–lamina associations are particularly heterogeneous between single cells compared with other stages (Fig. 1d). Moreover, we found that LAD profiles between cells from the same embryo are more similar (Extended Data Fig. 2c), suggesting that LADs are partially inherited from the zygote. However, we cannot exclude that this is related to slight variations in the volumes of injected Dam construct per embryo.

Lastly, by examining the CF distribution per chromosome, we found that genomic regions proximal to the centromere showed unusually high CF values, specifically at the 2-cell stage (Extended Data Fig. 2d,e). This suggests that centromeric regions tend to associate with the lamina in a more uniform manner across cells, despite the overall high LAD variability. This feature is unique to the totipotent 2-cell stage and coincides with dramatic changes in centromere organization in the nucleus[20,21].

LAD variability is higher for the paternal allele

Previous work has reported allelic differences in genome–lamina association up to the 8-cell stage[1]. This prompted us to investigate single-cell LAD profiles on the maternal and paternal alleles of mice with a hybrid background (B6CBAF1/J females and CAST/EiJ males). For mESCs, a hybrid strain of CAST/EiJ × 129Sv was used. These crosses yielded high-quality allele-specific single-cell LAD profiles, which revealed allelic asymmetry across single cells (Fig. 1e and Extended Data Fig. 3a–c). Moreover, in zygotes, 2-cell and 8-cell embryos, the paternal genome occupies a larger portion of the nuclear periphery compared with the maternal genome, whereas in mESCs LAD coverage is equal between alleles (Extended Data Fig. 3d).

Strikingly, we observed a profound discrepancy in the level of variability between alleles: whereas in zygotes, maternal LADs are more variable than paternal LADs, this trend is clearly inverted at the 2-cell and 8-cell stages (Fig. 1f). This is in contrast to mESCs, which show similar levels of cell-to-cell variability between both alleles. Interestingly, both alleles showed higher CF values at the centromeric regions of chromosomes, indicating that these regions are more consistently associated with the NL (Extended Data Fig. 3e,f).

Overall, these results indicate that paternal LADs contribute most to the unusually high cell-to-cell variability in the 2-cell and 8-cell embryo.

LAD variability is not reflected in transcriptional changes

Genome–lamina associations are typically associated with heterochromatic features and low gene expression. We therefore wondered whether variable genome–lamina positioning impacts chromatin state or gene expression. To answer this question, we made use of the combined genomic and transcriptomic readout of our single-cell data (Fig. 1a). Surprisingly, cells in which a gene contacted the NL showed expression levels comparable with cells from the same stage in which the same gene was not in contact with the NL (Extended Data Fig. 4a), arguing that LAD variation has no detectable consequences for gene expression.

To determine whether other chromatin features display similar variability across cells, we used EpiDamID[22], a single-cell DamID-based technique that has been adapted to detect histone marks. We chose to profile: (1) H3K9me3, which is often enriched in LADs; (2) H3K27me3, which plays an essential role in repressing genes during embryonic development; and (3) accessible chromatin, which tends to anti-correlate with LADs. To generate single-cell profiles of all three genomic features, the fusion constructs Dam–$Cbx1_{CD}$ (a tuple of the Cbx1 chromodomain), Dam–αH3K27me3 (scFv)[22] and the untethered Dam were used, respectively (Fig. 2a and Extended Data Fig. 4b,c).

In contrast to LADs, H3K27me3, H3K9me3 and accessible chromatin appeared to have a more uniform distribution across single cells (Fig. 2a (highlighted) and Extended Data Fig. 4d). To reliably compare levels of cell-to-cell variability for the different chromatin features,

https://doi.org/10.1038/s41588-024-01902-8

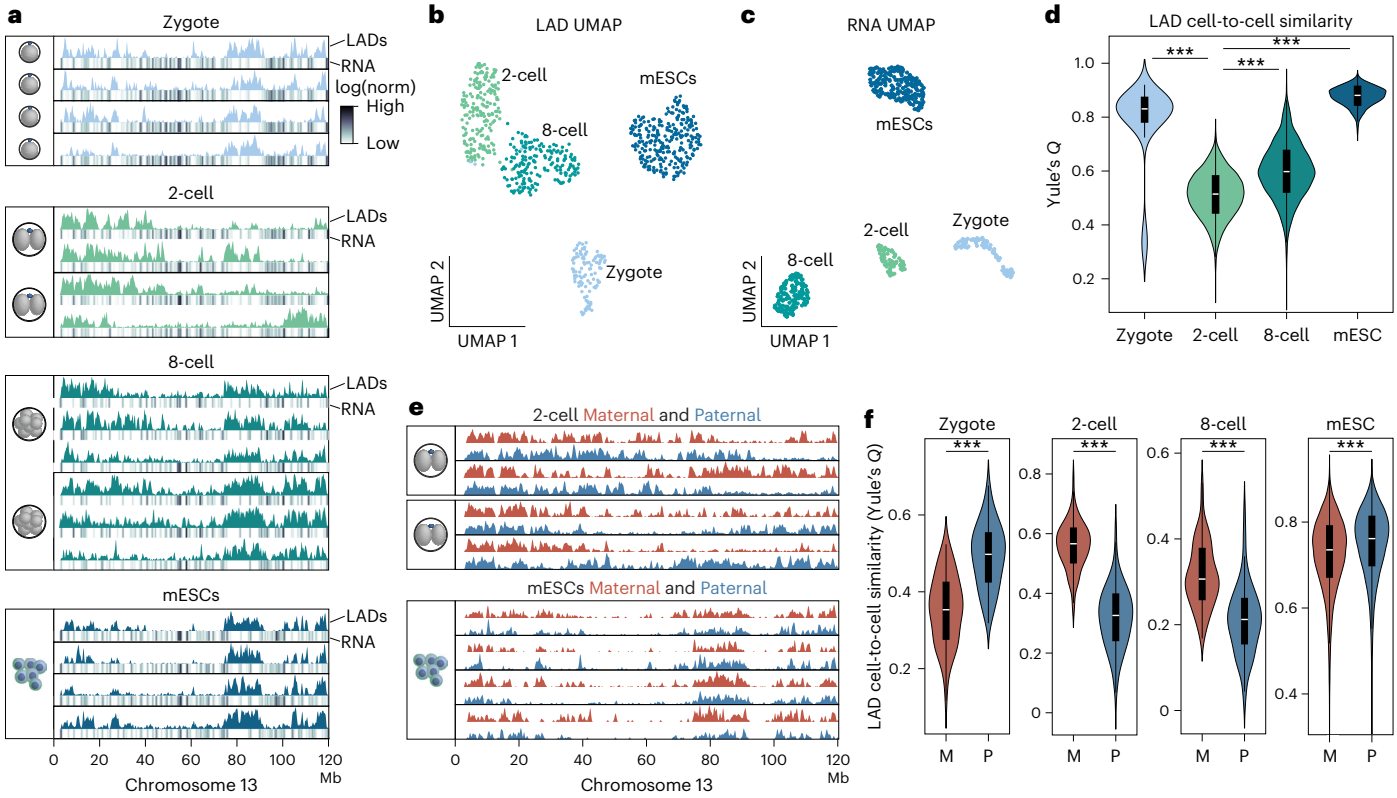

Fig. 1 | Genome–lamina contacts at the 2-cell stage are highly variable between single cells. a, Examples of LAD single-cell profiles (RPKM) and corresponding gene expression track (log-transformed depth-normalized (log(norm)) values scaled to maximum value per sample) across the entire chromosome 13 at different developmental stages and in mESCs. Single-cell profiles derived from the same embryo are grouped. **b**, UMAP based on Dam–LMNB1 single-cell readout ($n = 755$). **c**, Single-cell UMAP based on transcriptional readout of the cells in **b** passing transcriptional thresholds ($n = 482$). **d**, Distributions of cell-to-cell similarity (Yule's Q) of binarized single-cell Dam–LMNB1 data for zygote ($n = 253$ cell pairs, $^{***}P < 1 \times 10^{-100}$), 2-cell ($n = 17{,}020$ cell pairs), 8-cell ($n = 4{,}950$ cell pairs, $^{***}P < 1 \times 10^{-100}$) and mESC ($n = 15{,}356$ cell pairs, $^{***}P < 1 \times 10^{-100}$). **e**, 2-cell and mESC example single-cell LAD profiles split in maternal (red) and paternal (blue) alleles. For the 2-cell stage, allele-specific profiles from the same embryo are grouped. **f**, Distributions of cell-to-cell similarity (Yule's Q) of binarized allelic single-cell Dam–LMNB1 data for zygote ($n = 78$ cell pairs, $^{***}P = 8.4 \times 10^{-16}$), 2-cell stage ($n = 210$ cell pairs, $^{***}P = 4.8 \times 10^{-62}$), 8-cell stage ($n = 136$ cell pairs, $^{***}P = 2.2 \times 10^{-14}$) and mESC ($n = 29{,}161$ cell pairs, $^{***}P < 1 \times 10^{-100}$). Statistical testing was performed with a two-sided Mann–Whitney U-test. Boxplots in **d** and **f** show median values (white line), interquartile range (IQR, black box) and the range of all data points within 1.5× IQR (whiskers). M, maternal; P, paternal.

we normalized the cell-to-cell similarity scores (Extended Data Fig. 4b and Methods) and confirmed that LADs are more variable compared with H3K9me3, H3K27me3 and accessible chromatin (Fig. 2b). The results indicate that unlike LADs, these chromatin features are rather constant between individual cells, although some variability may still exist at a finer resolution. It is therefore unlikely that heterogeneity in chromatin state causes or is the result of LAD cell-to-cell variability at the 2-cell stage.

Regions that dissociate from the NL are H3K27me3-rich

In addition to high levels of cell-to-cell LAD variability, overall LAD patterns are highly atypical during the first cleavage stages: a large proportion of genomic regions associate or dissociate with the lamina uniquely in early embryos[1]. Interestingly, we noticed a striking relationship between atypical LADs and noncanonical broad H3K27me3 domains (Fig. 2a). To pursue this observation, we compared the 2-cell and mESC LADs in the context of 2-cell noncanonical H3K27me3 (ncH3K27me3) domains obtained from publicly available chromatin immunoprecipitation sequencing (ChIP-seq) data[13]. Interestingly, we found that regions with high H3K27me3 levels are depleted of LADs at the 2-cell stage, whereas these same regions strongly associate with the NL in mESCs (Fig. 2c,d).

We next clustered all genomic regions based on allele-resolved genome–lamina association and H3K27me3 values across all stages, and identified six genomic clusters (Fig. 2e and Extended Data Fig. 4e). To relate these clusters to different chromatin states, we also projected data from multiple ChIP-seq published datasets onto the clustering[10–13,23] (Extended Data Fig. 4e and Supplementary Table 3).

We confirmed the presence of genomic regions that are strongly associated with the lamina in mESCs, but lack lamina association in the early embryo, particularly on the maternal allele (cluster 2; Fig. 2e,f and Extended Data Fig. 4e). Regions that specifically lacked genome–lamina association in early development are instead strongly enriched for H3K27me3 and H3K9me3. These chromatin states are unique to early development, because these regions are lamina-associated and depleted of H3K27me3 and H3K9me3 in mESCs (Fig. 2e and Extended Data Fig. 4e). Moreover, they feature characteristics of typical LADs, such as low gene density, high density of long interspersed nuclear elements L1 and high A/T content (Extended Data Fig. 4f–h). We therefore termed these regions embryonic transient inter-LADs (ET-iLADs).

In addition to ET-iLADs, we identified five clusters with distinct lamina association and H3K27me3 enrichment. Constitutive LADs (cluster 1) are characterized by strong lamina association and low H3K27me3 across all stages. Embryonic transient LADs (cluster 3) are typified by genome–lamina associations unique to cleavage-stage embryos (Fig. 2e–f and Extended Data Fig. 4e). Similarly, paternal-specific LADs (cluster 4) are exclusively enriched on the paternal allele at 2-cell and 8-cell stages, with high levels of H3K27me3 on the maternal allele,

https://doi.org/10.1038/s41588-024-01902-8

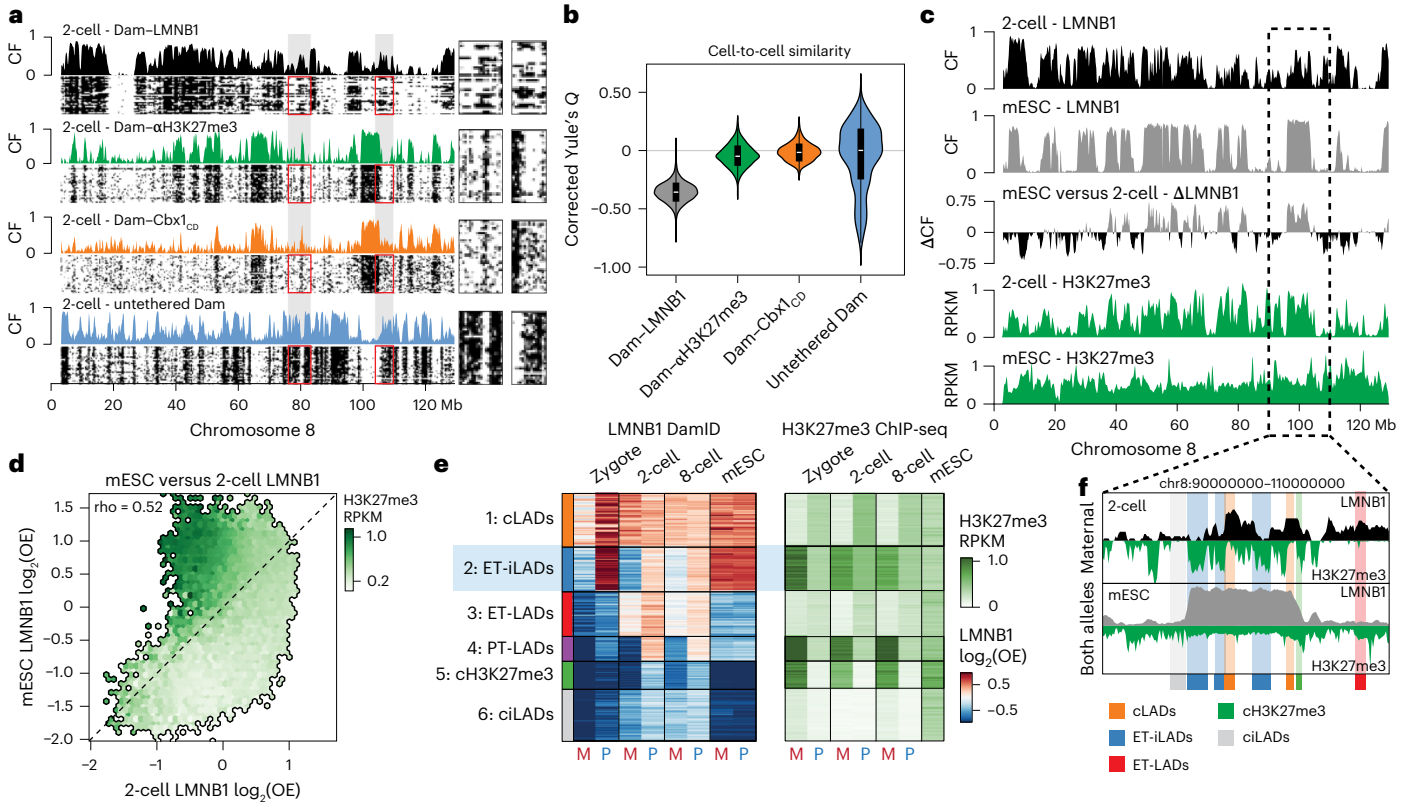

Fig. 2 | ET-iLADs that specifically detach from the NL in early embryos are enriched in H3K27me3. a, Binarized single-cell profiles for Dam–LMNB1, Dam–αH3K27me3 and Dam–Cbx1$_{CD}$ in 2-cell embryos across the entire chromosome 8, ordered by decreasing unique number of GATCs. The 30 richest cells are shown per condition. Corresponding CF tracks are shown above each heatmap. Gray boxes highlight example regions with variable genome–lamina association, but uniform enrichment of the other chromatin features. Cut-outs on the right show the same regions at greater magnification. **b**, Distributions of cell-to-cell similarity scores (corrected Yule's *Q*) per construct for Dam–LMNB1 (n = 19,306 cell pairs), Dam–αH3K27me3 (n = 435 cell pairs), Dam–Cbx1$_{CD}$ (n = 666 cell pairs) and untethered Dam (n = 2,926 cell pairs). A value of zero indicates a level of similarity that is expected based on technical noise, greater and smaller values indicate higher and lower similarity, respectively. Boxplots show median values (white line), IQR (black box) and the range of all data points within 1.5× IQR (whiskers). **c**, LMNB1 CF profiles and differential CF profile between mESC and 2-cell stage along chromosome 8. Publicly available H3K27me3 ChIP-seq data profiles of the 2-cell stage and mESCs are also shown[13]. The dashed box highlights an example with low CF and high H3K27me3 at the 2-cell stage. **d**, Genome-wide comparison between mESC and 2-cell LMNB1 DamID CF values in 100 kb bins. Color intensity refers to average H3K27me3 RPKM values obtained from publicly available ChIP-seq data[13]. Correlation was determined using Spearman's rank correlation coefficient (rho = 0.52, $P < 1 \times 10^{-100}$, n = 23,751 bins). **e**, Clustering of 100 kb genomic bins based on their allelic LMNB1 and H3K27me3 ChIP-seq values[13] at different embryonic stages and in mESCs. Left: LMNB1 CF values from both the maternal (M) and paternal (P) alleles across the different stages. Right: H3K27me3 ChIP-seq values. Blue shading is used to highlight ET-iLADs. **f**, Genomic region with examples of five of the genomic clusters identified in **e**. Mirror profiles show LMNB1 values (DamID) are given on the top and H3K27me3 (ChIP-seq[13]) on the bottom for the 2-cell stage (maternal allele) and mESCs (both alleles).

further demonstrating the antagonistic relationship between these chromatin types in the early embryo. Both paternal-specific LADs and embryonic transient LADs represent genomic regions that associate with the lamina only in the context of preimplantation development and score lower on classical LAD features, including low long interspersed nuclear element L1 density, low A/T content and high gene density (Extended Data Fig. 4f–h). Finally constitutive iLADs (cluster 6) and canonical H3K27me3 (cH3K27me3, cluster 5) have little to no lamina association throughout development. cH3K27me3 regions are enriched for known Polycomb-regulated genes and show high levels of H2AK119ub1 (Extended Data Fig. 4f,e), a histone post-translational modification laid down by Polycomb repressive complex 1 (PRC1). Constitutive iLADs are enriched instead for features of euchromatin, such as H3K4me3, H3K27ac, short interspersed nuclear elements and high gene density (Extended Data Fig. 4e–g).

Together these results indicate that LADs are extensively rewired during early development and show unique relationships to other chromatin features. Most notably, ET-iLADs specifically detach from the NL during the first days of embryonic development, coinciding with the presence of noncanonical H3K27me3.

H3K27me3 sequesters genomic regions away from the NL

The inverse relationship between genome–lamina association and ncH3K27me3 domains, prompted us to test this relationship directly. To this end, we depleted H3K27me3 in early development using a maternal knockout of *Eed* (*Eed* mKO), an essential component of PRC2 that deposits H3K27me3. This mutation is acquired in growing oocytes of *Eed*$^{fl/fl}$;*Gdf9*^{Cre} female mice and results in H3K27me3 loss from the oocyte up to the 8-cell stage[24,25] (Extended Data Fig. 5a). Embryos obtained from crosses with *Eed*$^{fl/fl}$ mothers were used as a control.

We performed scDam&T-seq in *Eed* mKO and control 2-cell embryos to uncover the effect of H3K27me3 loss on LADs. We used hybrid crosses between C57BL/6J females and JF1/MsJ males. Comparison of LAD profiles between the two conditions showed extensive LAD changes upon H3K27me3 depletion (Fig. 3a and Extended Data Fig. 5b). Notably, gains in genome–lamina associations upon *Eed* mKO correspond to patterns of H3K27me3 enrichment in wild-type (WT) 2-cell embryos, indicating that these regions are relocated to the NL in the *Eed* mKO condition (Fig. 3a,b and Extended Data Fig. 5c).

We then asked how the genomic clusters identified above were affected by Eed depletion. Indeed, the clusters that gained

https://doi.org/10.1038/s41588-024-01902-8

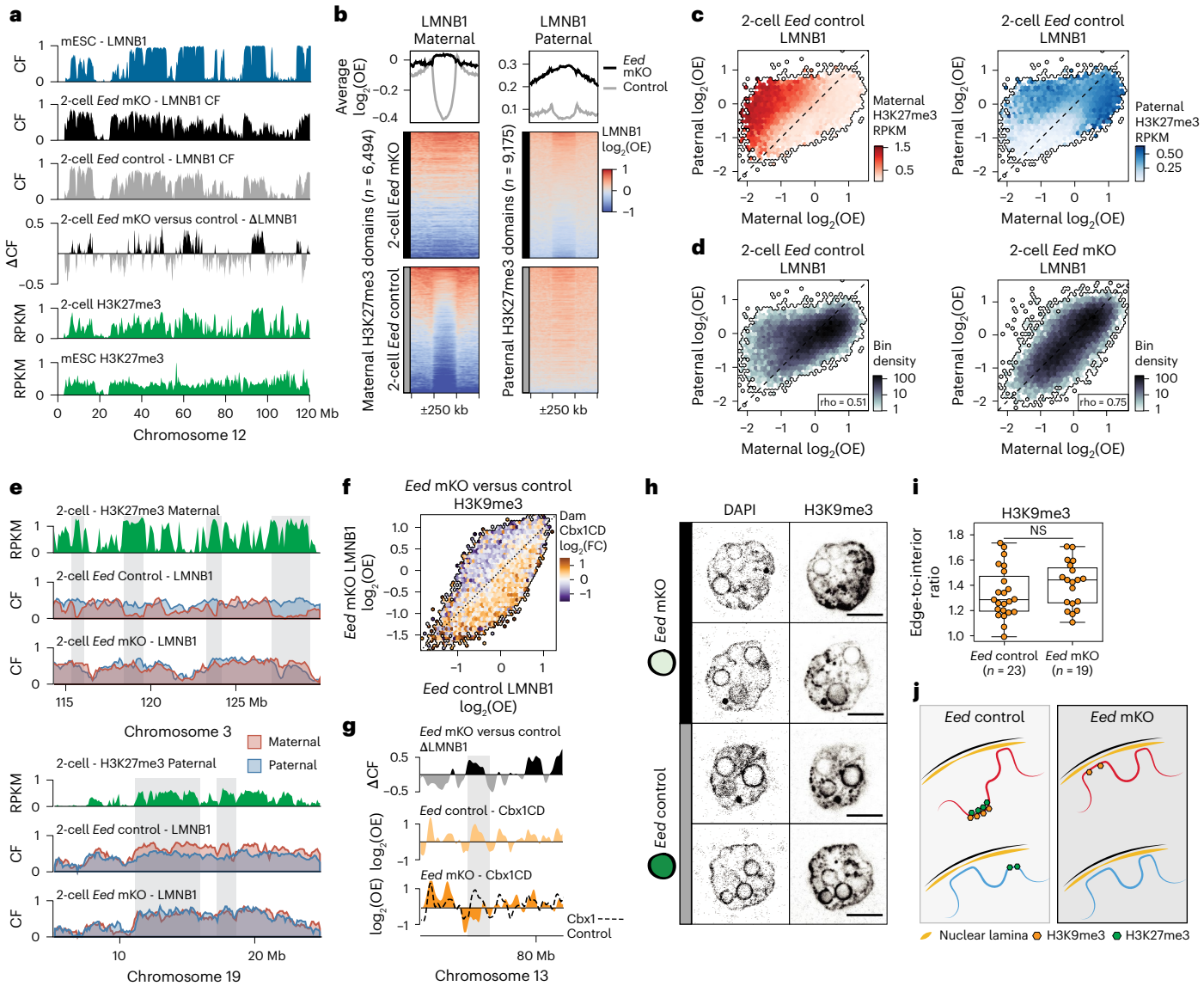

Fig. 3 | H3K27me3 antagonizes genome–lamina association during early development. a, LMNB1 profiles of control and *Eed* mKO 2-cell embryos and mESC, differential LMNB1 enrichment of *Eed* mKO versus control and H3K27me3 profiles (ChIP-seq[13]) over chromosome 12. **b**, Enrichment plot showing maternal (left) and paternal (right) LMNB1 enrichment of *Eed* mKO and control 2-cell embryos over H3K27me3 domains from the same allele and surrounding 250 kb. Heatmaps show LMNB1 signal per domain, whereas line plots show average enrichment over all domains. **c**, Comparison of maternal and paternal LMNB1 $\log_2$ observed-over-expected ($\log_2$(OE)) in 100 kb bins. The color indicates the average maternal (left, red) and paternal (right, blue) H3K27me3 RPKM values[13]. **d**, Comparison of paternal and maternal LMNB1 $\log_2$(OE) in control (left, rho = 0.51, $P < 1 \times 10^{-100}$, n = 19,869 100 kb bins) or *Eed* mKO (right, rho = 0.75, $P < 1 \times 10^{-100}$, n = 19,869 100 kb bins) embryos. Correlations were computed using Spearman's rank-order correlation. **e**, Example genomic regions where a reduction of LMNB1 allelic asymmetry is observed in regions enriched for maternal-specific H3K27me3 (upper) or paternal-specific H3K27me3 (lower). **f**, Comparison of LMNB1 $\log_2$(OE) in the *Eed* mKO and control embryos. Color intensity refers to the $\log_2$(fold change) in Dam–$Cbx1_{CD}$ (H3K9me3) enrichment between the two conditions. **g**, Example genomic region where the differential LMNB1 enrichment between the *Eed* mKO and control is plotted, as well as the Dam–$Cbx1_{CD}$ (H3K9me3) $\log_2$(OE) of both conditions separately. The Dam–$Cbx1_{CD}$ of the control is also plotted as a dashed line on the *Eed* mKO profile for reference. A shaded box highlights a region that gains genome–lamina associating in the *Eed* mKO while showing a loss in Dam–$Cbx1_{CD}$ enrichment. **h**, DAPI and immunostaining of H3K9me3 in 2-cell *Eed* mKO or *Eed* control embryos (scale bar, 10 µm). **i**, Quantification of the radial (1 µm) enrichment of H3K9me3 relative to the rest of the nucleus for the immunostaining in **h**. Significance was computed using Welch's two-sided t-test (P = 0.23, *Eed* control n = 23 nuclei, *Eed* mKO n = 19 nuclei). Data are from one biological replicate. Boxplots show median values (black line), IQR (black box) and the range of all data points within 1.5× IQR (whiskers). **j**, Model that illustrates the effect of H3K27me3 depletion in *Eed* mKO embryos. FC, fold change; NS, not significant.

genome–lamina associations corresponded to H3K27me3-rich regions in the WT 2-cell embryo, particularly ET-iLADs (Extended Data Fig. 5d). Strikingly, the resulting 2-cell stage LAD patterns in the *Eed* mKO condition strongly resembled genome–lamina associations in mESCs (Extended Data Fig. 5d), suggesting that upon loss of H3K27me3 LADs revert to their canonical state. Therefore, these findings show that H3K27me3 or PRC2 plays a key role in determining the atypical LAD organizations during early developmental stages.

Allelic LAD differences are reduced upon H3K27me3 depletion

Because both LADs and H3K27me3 show high allelic asymmetry in early developmental stages[1,26], we hypothesized that these two observations could be related. Comparison between maternal and paternal

LADs showed that regions with a paternal bias in lamina association are H3K27me3-rich on the maternal allele (Fig. 3c (left)). Conversely, a maternal bias in LADs is mirrored by paternal H3K27me3 enrichment, albeit less pronounced, likely caused by overall lower paternal H3K27me3 levels (Fig. 3c (right)). Interestingly, removal of H3K27me3 resulted in increased similarity between parental LAD patterns in *Eed* mKO embryos compared with controls (Fig. 3d,e). This increase in allelic concordance was only apparent in regions enriched in H3K27me3, whereas regions with low H3K27me3 levels remained similar (Extended Data Fig. 5e).

These results show that noncanonical distributions of H3K27me3 dictate allelic LAD asymmetry during early mouse development.

H3K9me3 does not cause relocation to the NL upon H3K27me3 loss

Given the extensive overlap between H3K27me3 and H3K9me3 in preimplantation embryos (Fig. 2a and Extended Data Fig. 4e), we wondered whether in the absence of H3K27me3, H3K9me3 could be involved in repositioning genomic regions to the lamina. To this end, we performed scDam&T-seq using the Dam–$Cbx1_{CD}$ construct to label H3K9me3-enriched regions in the *Eed* mKO condition. Surprisingly, we found that the genomic regions that gain lamina association in the absence of H3K27me3 tend to have reduced H3K9me3 levels compared with controls (Fig. 3f,g and Extended Data Fig. 5f). Concordantly, we found no increase in H3K9me3 signal at the nuclear periphery in *Eed* mKO embryos compared with controls (Fig. 3h–i). These observations preclude a role for H3K9me3 re-establishing canonical LADs in the absence of H3K27me3. This notion is further supported by the observation that the paternal genome gains genome–lamina association in *Eed* mKO embryos, even though paternal H3K9me3 is largely absent at this stage[11] (Extended Data Fig. 4e).

Together, these results show that *Eed* and H3K27me3 depletion causes re-establishment of canonical LADs through an H3K9me3-independent mechanism (Fig. 3j).

Association with the NL is not sufficient to remove H3K27me3

Having uncovered a strong antagonistic relationship between H3K27me3 and nuclear localization of the genome, we wondered whether forcing ncH3K27me3 regions to the NL would have an effect on chromatin state and embryonic development. To this end, we designed constructs in which a triplet of Cbx7 chromodomains, which specifically bind H3K27me3 (ref. 22), was fused to different inner nuclear membrane proteins: Lap2β, Emerin (Emd) or Lamin B receptor (Lbr). All three constructs showed increased lamina association of H3K27me3 domains, with Cbx7–Lap2β fusion showing the most pronounced tethering effect (Fig. 4a and Extended Data Fig. 6a). This effect was not observed in the untethered Lap2β condition. The changes in genome–lamina association caused by H3K27me3 tethering did not result in large-scale chromatin accessibility changes (Extended Data Fig. 6b).

To determine allelic-specific effects of the tethering, we used hybrid embryos (B6CBAF1/J × CAST/EiJ) and calculated allele-resolved genome–lamina enrichment over H3K27me3 domains. Although control Lap2β embryos displayed low lamina association over H3K27me3-rich regions, the tethering construct showed a clear enrichment (Fig. 4b and Extended Data Fig. 6c,d). ET-iLADs, which are characterized by high H3K27me3 enrichment and typical LAD features, were most consistently tethered to the NL (Fig. 4c).

Similar to *Eed* mKO embryos, *Cbx7–Lap2β*-injected embryos showed reduced parental LAD asymmetry. However, a higher degree of allelic asymmetry remained, because of unequal tethering of regions with allele-specific H3K27me3 enrichment (Extended Data Fig. 6e,f).

Next, we tested whether the presence of H3K27me3 was compatible with NL localization. We found a clear increase in H3K27me3 localization at the nuclear periphery in *Cbx7–Lap2β*-injected 2-cell embryos in comparison with uninjected or *Lap2β*-injected embryos (Fig. 4d and Extended Data Fig. 6g), suggesting that H3K27me3 is retained upon forced relocation to the NL.

We previously observed that H3K9me3 levels are reduced in the *Eed* mKO condition (Fig. 3f-g and Extended Data Fig. 5f), which could be caused by H3K27me3 loss or repositioning of ET-iLADs to the NL. To disentangle these variables, we performed immunofluorescence staining for H3K9me3 in *Cbx7–Lap2β* embryos, in which ET-iLADs are also relocated to the NL while retaining H3K27me3. Unlike in the *Eed* mKO embryos, we observed a strong enrichment of H3K9me3 at the nuclear periphery upon tethering H3K27me3 domains to the NL (Fig. 4e and Extended Data Fig. 6h). Therefore, H3K9me3 reduction at ET-iLADs upon *Eed* mKO does not appear to be caused by the change in nuclear localization of these regions.

Eed mKO has been described to result in the reduction of interactions between Polycomb-associated domains (PADs), transient H3K27me3-rich three-dimensional contact domains observed in early embryos[26]. To investigate whether H3K27me3 tethering at the NL could disrupt PAD–PAD interactions, we made use of our single-cell Dam–LMNB1 data to infer chromatin organization[19] (Extended Data Fig. 6i and Methods). This demonstrated that the Cbx7–Lap2β retained stronger PAD–PAD interactions compared with *Eed* mKO embryos (Extended Data Fig. 6j).

Finally, we wished to test the effect of tethering H3K27me3 regions to the NL on embryonic development. Performing a viability experiment up to the blastocyst stage, we found no apparent effect on embryo development or gene expression (Extended Data Fig. 6k,l).

In summary, these results show that we have developed a strategy that successfully tethers H3K27me3 to the lamina in the early embryo. With this system, we disentangled the roles of H3K27me3 loss and LAD rewiring observed in *Eed* mKO embryos. We find that PRC2 and H3K27me3 depletion, and not the change in nuclear localization, causes H3K9me3 decrease and loss of higher-order chromatin structures in *Eed* mKO conditions.

H3K27me3 and NL affinity shape atypical LADs

Eed mKO and Cbx7–Lap2β embryos both showed the strongest gain in genome–lamina association in ET-iLADs (Fig. 4c and Extended Data Fig. 5d). These regions are characterized by: (1) being at the NL in other cell types; (2) having high levels of H3K27me3, specifically in the early embryo; and (3) displaying typical sequence traits of LADs (Extended Data Fig. 4f–h). This suggests the presence of an underlying affinity encoded in the DNA sequence that is counteracted by the presence of H3K27me3 in early embryogenesis.

We set out to define a metric that can represent genome–lamina affinity inherent to the DNA sequence. Lamin proteins have been shown to bind A/T-rich sequences in vitro[27] and LADs are notoriously A/T rich[28], suggesting a link between A/T content and NL affinity. In addition, it has been suggested that the zygotic LAD profile represents a 'default' lamina-association state encoded in the DNA sequence itself[1]. Indeed, the correlation between A/T content and zygotic genome–lamina association was very high, further indicating that A/T content is a good metric for intrinsic NL affinity (Extended Data Fig. 7a).

To evaluate the joint effects of intrinsic NL affinity and H3K27me3 on LADs at the 2-cell stage, we divided the genomic bins into nine categories based on their A/T content (low, mid and high) and allele-specific H3K27me3 level (low, mid and high) (Extended Data Fig. 7b–d). When considering maternal genome–lamina association, we found that genomic regions with low H3K27me3 and high NL affinity show the strongest genome–lamina association. Centromere-proximal regions are strongly represented in this category, explaining their unusually strong genome–lamina association at the 2-cell stage (Extended Data Fig. 2d,e). At each level of NL affinity, genome–lamina association tends to diminish with increasing levels of H3K27me3 (Fig. 5a,b (left) and Fig. 5c,d). These results indicate that genome–lamina association at the 2-cell stage is determined by the presence of two antagonistic

https://doi.org/10.1038/s41588-024-01902-8

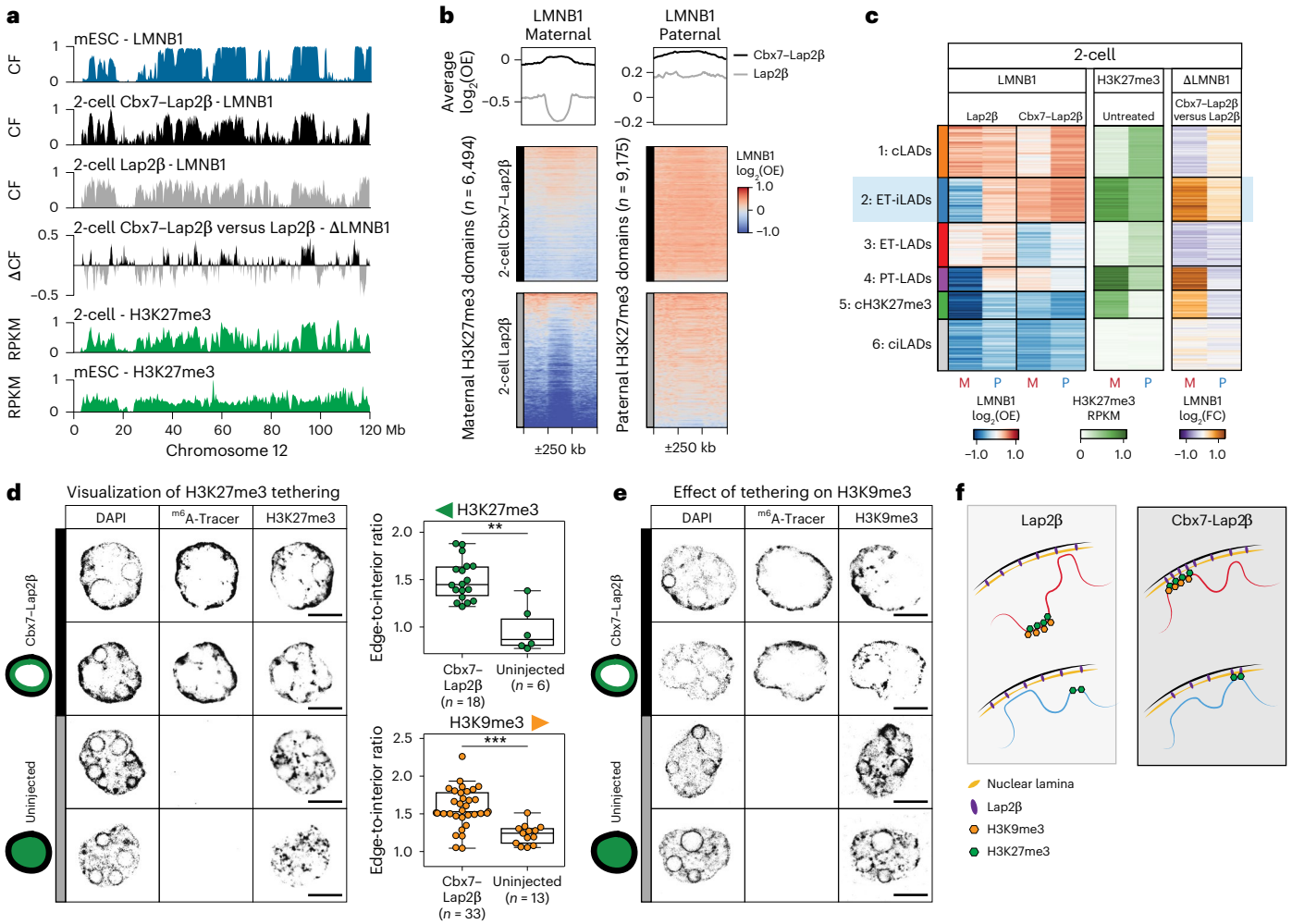

Fig. 4 | H3K27me3 is retained when forced to associate to the lamina. a, LMNB1 profiles of *Lap2β* and *Cbx7–Lap2β*-injected 2-cell embryos, differential LMNB1 enrichment between the two conditions, mESC LMNB1 profile and H3K27me3 profiles (ChIP-seq[13]) over chromosome 12. **b**, Enrichment plot showing maternal (left) and paternal (right) LMNB1 enrichment for Cbx7–Lap2β and Lap2β conditions over H3K27me3 domains from the same allele and surrounding 250 kb. Heatmaps show LMNB1 signal per domain, and line plots show average enrichment over all domains. **c**, Heatmap showing allelic LMNB1 values across genomic clusters (as in Fig. 2e) for *Lap2β* and *Cbx7–Lap2β*-injected 2-cell embryos. H3K27me3 from ChIP-seq data[13] at the 2-cell stage is shown for comparison. Blue shading is used to highlight ET-iLADs. **d**,**e**, DAPI immunostaining of the ^{m6}A-Tracer, and immunostaining of H3K27me3 (**d**) or H3K9me3 (**e**) in 2-cell Cbx7–Lap2β and Lap2β embryos (scale bar, 10 µm). Detection of ^{m6}A-Tracer signal indicates successful injection of the Dam–LMNB1 and Cbx7–Lap2β constructs (Methods). Right of **d**: quantification of the radial (1 µm) enrichment of H3K27me3 (upper) and H3K9me3 (lower) relative to the rest of the nucleus. Significance was computed using Welch's two-sided *t*-test (H3K27me3, $^{**}P = 1.6 \times 10^{-3}$, Cbx7–Lap2β $n = 18$ nuclei, uninjected $n = 6$ nuclei; H3K9me3, $^{***}P = 3.6 \times 10^{-7}$, Cbx7–Lap2β $n = 33$ nuclei, uninjected $n = 13$ nuclei). Data are from one biological replicate. Boxplots show median values (black line), IQR (black box) and the range of all data points within 1.5× IQR (whiskers). **f**, Model that illustrates the effect of H3K27me3 tethering during early development.

forces: the NL affinity encoded in the DNA sequence countered by a repellent effect of H3K27me3 presence.

Next, we determined the changes in genome–lamina association across the different genome categories upon H3K27me3 depletion (*Eed* mKO) and peripheral tethering (Cbx7–Lap2β). As expected, genome–lamina association in the *Eed* mKO 2-cell nucleus is no longer influenced by H3K27me3 and becomes solely dictated by NL affinity (Fig. 5a (right) and Fig. 5c). In the *Cbx7–Lap2β*-injected embryos, however, lamina association was strongest for regions with both high NL affinity and high H3K27me3, suggesting that the two features reinforced each other to bring genomic regions to the NL (Fig. 5b (right) and Fig. 5d). This indicates that expression of Cbx7–Lap2β abrogated the repellent properties of H3K27me3 and converted it to a positive force in NL tethering.

Surprisingly, we also observed a loss of genome–lamina association for H3K27me3-low regions in *Eed* mKO and Cbx7–Lap2β conditions (Fig. 5a,d). This is likely caused by competition for the limited space available at the NL, as demonstrated by the relatively constant genomic fraction associating with the lamina across conditions (Extended Data Fig. 7f).

Next, we wondered whether the opposing effects of NL affinity and H3K27me3 could play a role in the unusually high LAD variability that characterizes the preimplantation embryo. Indeed, both removing H3K27me3 and tethering H3K27me3 regions to the NL showed a pronounced reduction in paternal LAD variability, whereas variability on the maternal genome remained largely unaffected (Fig. 5e). In the first instance, this was a surprising result, given the rather low levels of H3K27me3 on the paternal allele compared with the maternal allele[13] (Fig. 2e). However, we observed that a large number of paternal LADs at the 2-cell stage are characterized by intermediate levels of H3K27me3 and mid to high NL affinity (Fig. 5f and Extended Data Fig. 7d (right)). This means that, unlike the maternal allele, a large part of the paternal

https://doi.org/10.1038/s41588-024-01902-8

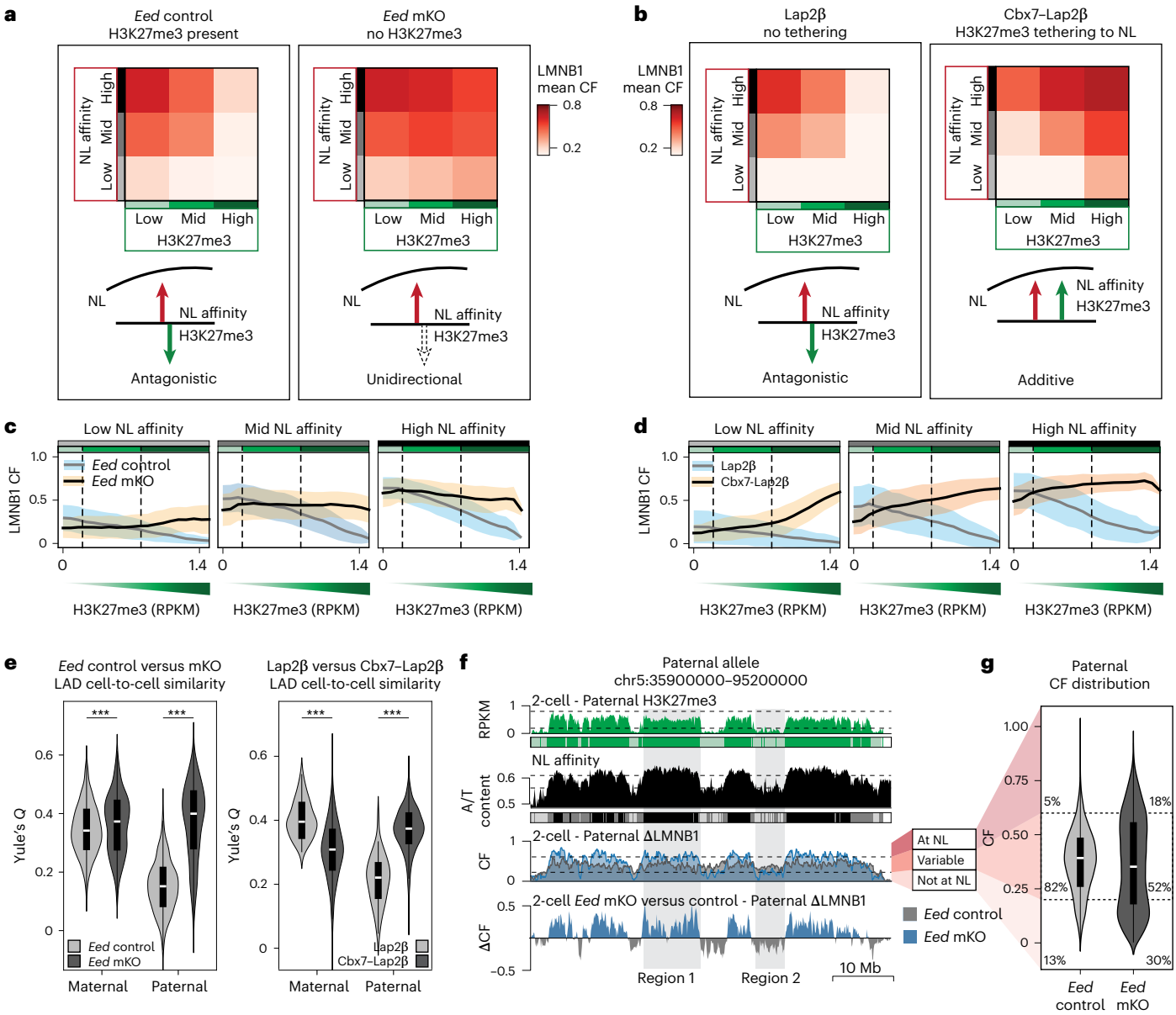

Fig. 5 | Antagonism between intrinsic NL affinity and H3K27me3 levels dictates genome–lamina association and leads to high LAD heterogeneity between cells of early embryos. a,**b**, Heatmap of average maternal LMNB1 CF values of *Eed* control and *Eed* mKO 2-cell embryos (**a**) or *Lap2β* and *Cbx7–Lap2β*-injected embryos (**b**) across nine categories of varying NL affinity and H3K27me3 level (defined in Extended Data Fig. 7d). **c**,**d**, LMNB1 CF values of *Eed* control and *Eed* mKO (**c**) or Lap2β and Cbx7–Lap2β conditions (**d**) across increasing 2-cell H3K27me3 RPKM values. The line indicates the mean and the shaded area indicates the standard deviation. **e**, Allele-specific distribution of the cell-to-cell similarity (Yule's *Q*) in *Eed* control and *Eed* mKO (left: maternal $^{***}P = 3.2 \times 10^{-4}$, paternal $^{***}P < 1 \times 10^{-100}$) and *Lap2β* and *Cbx7–Lap2β*-injected embryos (right: maternal $^{***}P = 3.1 \times 10^{-13}$, paternal $^{***}P = 1.7 \times 10^{-23}$). *Eed* control, $n = 1{,}275$ cell pairs; *Eed* mKO, $n = 465$ cell pairs; Lap2β, $n = 45$ cell pairs; Cbx7–Lap2β, $n = 741$ cell pairs. Significance between conditions was computed with the two-sided Mann–Whitney *U*-test. **f**, Example profile on chromosome 5 of paternal H3K27me3, NL affinity and paternal LMNB1 profiles of *Eed* control and mKO. Color-coded boxes under H3K27me3 and NL affinity refer to the different levels pictured in **a** and Extended Data Fig. 7d. Region 1 highlights an example in which genome–lamina association is increased in *Eed* mKO, whereas region 2 highlights an example in which it is decreased. Both regions show reduced variability. **g**, Distribution of paternal LMNB1 CF values in *Eed* control and *Eed* mKO embryos. Percentages indicate, from top to bottom, the fraction of 100 kb genomic bins ($n = 20{,}715$) with high, intermediate and low CF values. Boxplots in **e** and **g** indicate median values (white line), IQR (black box) and the range of all data points within 1.5× IQR (whiskers).

genome is directly affected by the tug-of-war between intrinsic NL affinity and H3K27me3, resulting in high cell-to-cell variability. Using CF as a measure of LAD variability[19], we found that *Eed* mKO causes more consistent lamina association of regions on the paternal allele with mid to high NL affinity (Fig. 5f (region 1)). By contrast, regions with low NL affinity and low H3K27me3 levels are more consistently excluded from the NL, likely being outcompeted by higher NL affinity regions (Fig. 5f (region 2)). Thus, H3K27me3 depletion results in the overall reduction of intermediate CF values, indicative of high LAD variability in the paternal genome (Fig. 5g).

Together these results show that two antagonistic forces—inherent NL affinity and H3K27me3—constrained by the space available at the nuclear periphery, cause the unusually high variability of lamina association across cells of the totipotent embryo.

Discussion

Here, we have profiled LADs in single cells of preimplantation embryos and mESCs, and identified a potential mechanism for the atypical and allele-specific genome–lamina interactions during early development.

We showed that genomic positioning with respect to the nuclear periphery varies extensively across cells at the 2-cell stage. Although some level of single-cell variability is observed in other systems[18,19], the unusually high LAD heterogeneity in early development could be related to the totipotent nature of these stages. Interestingly, paternal zygotic LADs are not as variable, potentially because of either de novo establishment of LAD patterns in the absence of paternally inherited chromatin modifications or the maintenance of LAD patterns carried over from sperm, which have yet to be profiled.

On examining various chromatin marks and transcription, we did not observe variability at the same level as for LADs, indicating an unusual uncoupling between three-dimensional genome organization and gene regulation.

Broad noncanonical domains of maternal H3K27me3 form during oogenesis, persisting until the post-implantation stages[13]. Similarly, paternal H3K27me3 is rapidly redistributed after fertilization to form broad noncanonical domains. Here, we find that these noncanonical H3K27me3 regions overlap with canonical LADs and decrease genome–lamina association at the 2-cell stage, particularly on the paternal allele. Interestingly, it was previously shown that deposition of H2AK119ub1 and H3K27me3 at paternal peri-centromeric heterochromatin is dependent on the A/T-binding capacity of PRC1 component Cbx2 and could be inhibited by the presence of H3K9me3/heterochromatin protein 1β[29]. Because canonical LADs are very A/T rich and the paternal allele lacks H3K9me3 in zygote[11] (Extended Data Fig. 4f), the same mechanism could potentially explain the deposition of H3K27me3 in these regions.

Depletion of H3K27me3 in the 2-cell embryo via maternal KO of *Eed*, prompts ncH3K27me3 regions to become LADs, demonstrating that H3K27me3 antagonizes lamina association. In support of this finding, a recent study reported increased lamina association of B compartment regions rich in H3K27me3 upon inhibition of another PRC2 component, Ezh2, in K562 cells[30]. This antagonistic relationship could explain the massive rearrangements of paternal LADs between zygote and 2-cell stages[1], because this coincides with the establishment of paternal H3K27me3 (ref. 13).

Nuclear envelope proteins have been shown to interact with histone modifiers[31] and the NL environment is able to alter the activity of some promoters[31,32]. However, tethering of H3K27me3 to the nuclear periphery did not result in depletion of this mark, indicating that it is not inherently incompatible with the nuclear periphery environment.

The study of epigenetics, nuclear organization and transcription during the first days of embryonic development has greatly benefited from the development of new low-input technologies[8–13]. An overall view of noncanonical epigenetic features and major restructuring of genomic organization has emerged, but little is known about how these processes are connected and what their role in embryonic development may be. Here, we propose a model, whereby H3K27me3 antagonizes genome–lamina association during preimplantation development causing atypical organization, allelic asymmetry and cell-to-cell heterogeneity in genome–lamina association. We demonstrate that this interplay between Polycomb and genome–lamina association is mechanistically involved in the processes that so dramatically reorganize the nuclear architecture during preimplantation development.

Online content

Any methods, additional references, Nature Portfolio reporting summaries, source data, extended data, supplementary information, acknowledgements, peer review information; details of author contributions and competing interests; and statements of data and code availability are available at https://doi.org/10.1038/s41588-024-01902-8.

References

1. Borsos, M. et al. Genome-lamina interactions are established de novo in the early mouse embryo. *Nature* **569**, 729–733 (2019).
2. Burton, A. & Torres-Padilla, M. E. Chromatin dynamics in the regulation of cell fate allocation during early embryogenesis. *Nat. Rev. Mol. Cell Biol.* **15**, 723–734 (2014).
3. Guerreiro, I. & Kind, J. Spatial chromatin organization and gene regulation at the nuclear lamina. *Curr. Opin. Genet. Dev.* **55**, 19–25 (2019).
4. Kind, J. & van Steensel, B. Genome-nuclear lamina interactions and gene regulation. *Curr. Opin. Cell Biol.* **22**, 320–325 (2010).
5. van Steensel, B. & Belmont, A. S. Lamina-associated domains: links with chromosome architecture, heterochromatin, and gene repression. *Cell* **169**, 780–791 (2017).
6. Vogel, M. J., Peric-Hupkes, D. & van Steensel, B. Detection of in vivo protein–DNA interactions using DamID in mammalian cells. *Nat. Protoc.* **2**, 1467–1478 (2007).
7. Chen, Z., Djekidel, M. N. & Zhang, Y. Distinct dynamics and functions of H2AK119ub1 and H3K27me3 in mouse preimplantation embryos. *Nat. Genet.* **53**, 551–563 (2021).
8. Dahl, J. A. et al. Broad histone H3K4me3 domains in mouse oocytes modulate maternal-to-zygotic transition. *Nature* **537**, 548–552 (2016).
9. Liu, X. et al. Distinct features of H3K4me3 and H3K27me3 chromatin domains in pre-implantation embryos. *Nature* **537**, 558–562 (2016).
10. Mei, H. et al. H2AK119ub1 guides maternal inheritance and zygotic deposition of H3K27me3 in mouse embryos. *Nat. Genet.* **53**, 539–550 (2021).
11. Wang, C. et al. Reprogramming of H3K9me3-dependent heterochromatin during mammalian embryo development. *Nat. Cell Biol.* **20**, 620–631 (2018).
12. Zhang, B. et al. Allelic reprogramming of the histone modification H3K4me3 in early mammalian development. *Nature* **537**, 553–557 (2016).
13. Zheng, H. et al. Resetting epigenetic memory by reprogramming of histone modifications in mammals. *Mol. Cell* **63**, 1066–1079 (2016).
14. Guelen, L. et al. Domain organization of human chromosomes revealed by mapping of nuclear lamina interactions. *Nature* **453**, 948–951 (2008).
15. Biase, F. H., Cao, X. & Zhong, S. Cell fate inclination within 2-cell and 4-cell mouse embryos revealed by single-cell RNA sequencing. *Genome Res.* **24**, 1787–1796 (2014).
16. Shi, J. et al. Dynamic transcriptional symmetry-breaking in pre-implantation mammalian embryo development revealed by single-cell RNA-seq. *Development* **142**, 3468–3477 (2015).
17. Torres-Padilla, M. E., Parfitt, D. E., Kouzarides, T. & Zernicka-Goetz, M. Histone arginine methylation regulates pluripotency in the early mouse embryo. *Nature* **445**, 214–218 (2007).
18. Rooijers, K. et al. Simultaneous quantification of protein-DNA contacts and transcriptomes in single cells. *Nat. Biotechnol.* **37**, 766–772 (2019).
19. Kind, J. et al. Genome-wide maps of nuclear lamina interactions in single human cells. *Cell* **163**, 134–147 (2015).
20. Borsos, M. & Torres-Padilla, M. E. Building up the nucleus: nuclear organization in the establishment of totipotency and pluripotency during mammalian development. *Genes Dev.* **30**, 611–621 (2016).
21. Puschendorf, M. et al. PRC1 and Suv39h specify parental asymmetry at constitutive heterochromatin in early mouse embryos. *Nat. Genet.* **40**, 411–420 (2008).
22. Rang, F. J. et al. Single-cell profiling of transcriptome and histone modifications with EpiDamID. *Mol. Cell* **82**, 1956–1970. e14 (2022).

23. Wang, M., Chen, Z. & Zhang, Y. CBP/p300 and HDAC activities regulate H3K27 acetylation dynamics and zygotic genome activation in mouse preimplantation embryos. *EMBO J.* **41**, e112012 (2022).
24. Du, Z. et al. Allelic reprogramming of 3D chromatin architecture during early mammalian development. *Nature* **547**, 232–235 (2017).
25. Inoue, A., Chen, Z., Yin, Q. & Zhang, Y. Maternal Eed knockout causes loss of H3K27me3 imprinting and random X inactivation in the extraembryonic cells. *Genes Dev.* **32**, 1525–1536 (2018).
26. Du, Z. et al. Polycomb group proteins regulate chromatin architecture in mouse oocytes and early embryos. *Mol. Cell* **77**, 825–839.e7 (2020).
27. Ludérus, M. E., den Blaauwen, J. L., de Smit, O. J., Compton, D. A. & van Driel, R. Binding of matrix attachment regions to lamin polymers involves single-stranded regions and the minor groove. *Mol. Cell. Biol.* **14**, 6297–6305 (1994).
28. Meuleman, W. et al. Constitutive nuclear lamina–genome interactions are highly conserved and associated with A/T-rich sequence. *Genome Res.* **23**, 270–280 (2013).
29. Tardat, M. et al. Cbx2 targets PRC1 to constitutive heterochromatin in mouse zygotes in a parent-of-origin-dependent manner. *Mol. Cell* **58**, 157–171 (2015).
30. Siegenfeld, A. P. et al. Polycomb-lamina antagonism partitions heterochromatin at the nuclear periphery. *Nat. Commun.* **13**, 4199 (2022).
31. Briand, N. & Collas, P. Lamina-associated domains: peripheral matters and internal affairs. *Genome Biol.* **21**, 85 (2020).
32. Leemans, C. et al. Promoter-intrinsic and local chromatin features determine gene repression in LADs. *Cell* **177**, 852–864.e14 (2019).

Methods

Ethics statement

Animal experiments on WT mice were approved by the animal ethics committee of the Royal Netherlands Academy of Arts and Sciences (KNAW) under project license AVD801002016728 and study dossiers HI173301 and HI213301. Animal experiments on the *Eed* mKO and Eed control mouse strains were performed in accordance with Swiss animal protection laws (licenses 2569 and 3183, Gesundheitsdepartement Kanton Basel-Stadt, Veterinäramt, Switzerland) and institutional guidelines.

Cloning and RNA synthesis

The pRN3P–Dam–LMNB1 plasmid was described in ref. 1. pRN3P–Dam-only was fused to an N-terminal ERT2 sequence. The remaining Dam fusion constructs were cloned from plasmids described in ref. 22 into the same in vitro transcription vector (pRN3P)[1], linearized, purified using the QIAquick PCR Purification Kit (Qiagen) and transcribed using the T3 mMessage mMachine kit (Invitrogen, cat. no. AM1348) according to the manufacturer's instructions. The synthesized RNA was purified using the MEGAclear kit (Invitrogen, cat. no. AM1908) or the lithium chloride RNA precipitation method and eluted in 10 mM Tris–HCl buffer (pH 7.5) and 0.1 mM EDTA.

Tethering constructs were generated by cloning the Cbx7 triple chromodomain and C-terminal linker from the pCCL.PGK-(PD-CBX7)3x plasmid described in ref. 22 and fused to either the mouse Lap2β, Emerin or Lbr coding sequence at the C-terminal end.

Animal care and zygote injection

WT mouse embryos were collected from B6CBAF1/J females crossed with CAST/EiJ males for the hybrid experiments and B6CBAF1/J males for nonhybrid experiments. The *Eed* floxed mouse (*Eed*$^{fl/fl}$) was provided by S. H. Orkin. To obtain *Eed* maternal KO embryos or controls, we crossed *Eed*$^{fl/fl}$*;Gdf9-icre* (The Jackson Laboratory, cat. no. 011062) or *Eed*$^{fl/fl}$ females (on a C57BL/6J background), respectively, with JF1/MsJ WT males. All males used were under 12 months old.

For all crosses, 7–10-week-old females were superovulated by injecting pregnant mare serum gonadotropin (5 IU; MSD, cat. no. A207A01) and human chorionic gonadotropin (hCG, 5 IU; MSD, cat. no. A201A01). For in vitro fertilization, spermatozoa from JF1/MsJ males were capacitated in human tubal fluid medium (Merck Millipore, cat. no. MR-070-D) supplemented with 10 mg ml^{-1} albumin (HTF-BSA; Sigma, cat. no. A-3311) for 1 h preceding insemination. MII oocytes were collected in the insemination medium (HTF-BSA) and capacitated spermatozoa were added for fertilization. The insemination starting time point was termed 0 h post-fertilization.

When using standard mating, zygotes were injected approximately 24 h post-hCG.

For both in vitro fertilization and normal mating messenger RNA was microinjected in the cytosol of the zygote at 10 h post-fertilization. A full description of the constructs used, the corresponding concentrations and induction conditions is given in Supplementary Table 4.

Injected zygotes were cultured in KSOM medium for hybrid crosses (Sigma, cat. no. MR-106-D) or M16 medium (Sigma, cat. no. M7292) for nonhybrid crosses covered with mineral oil (Sigma, cat. no. M8410) at 37 °C with 5% CO_2 and 5% O_2 air.

To increase the quality of DamID signal, untethered Dam and Dam–$Cbx1_{CD}$ constructs were fused to an ERT2 domain so that the fusion protein would be translocated to the nucleus upon addition of 4-hydroxytamoxifen (Sigma, cat. no. SML1666) (Supplementary Table 4).

Embryo collection, dissociation and sorting

Embryos were collected by mouth pipetting at 29–31 h post-hCG for the zygote stage, 52–55 h post-hCG for the 2-cell stage and 75–78 h post-hCG for the 8-cell stage (Supplementary Table 4). The zona pellucida was removed using Tyrode's acid (Sigma, cat. no. T1788), washed in M2 medium (Sigma, cat. no. MR-015) and placed in TrypLE (Gibco, cat. no. 12605010) where embryos were dissociated into single cells one by one and placed in M2 medium before single-cell collection into a 384-well plate containing 5 µl of mineral oil and 100 nl of barcoded polyadenylated primers.

scDam&T-seq processing

All scDam&T-seq steps were performed as previously described[33] (see Supplementary Methods for more detailed information).

Immunofluorescence staining

After removal of the zona pellucida with Tyrode's acid, embryos were fixed in 4% paraformaldehyde in phosphate-buffered saline (PBS) at room temperature for 15 min and permeabilized in PBS with 0.5% Triton X-100 for 20 min, at room temperature. Embryos were then incubated with blocking solution (2% bovine serum albumin in PBS) for 1 h or more. Incubation with primary antibody and m6A-Tracer protein[34] was performed overnight at 4 °C. When m6A-Tracer protein was used, the overnight incubation was followed by a 1 h incubation at room temperature with anti-green fluorescent protein (anti-GFP) antibody. For all stainings, secondary antibodies incubations were also performed for 1 h at room temperature followed by DAPI staining with 3 µg ml^{-1} for 20 min. Samples were mounted on glass slides using a spacer and VECTASHIELD Antifade mounting medium (Vector Laboratories). Primary antibodies used were: rabbit anti-H3K27me3 (Cell Signaling Technology, cat. no. C36B11, lot 19) at 1:200, rabbit anti-H3K9me3 (Abcam, cat. no. ab8898, lot GR3281994-1) at 1:300 and chicken anti-GFP (Aves, cat. no. GFP-1020, lot GFP697986) at 1:1,000. Secondary antibodies were all used at 1:500: Alexa Fluor 488 goat anti-chicken (Invitrogen, cat. no. A11039, lot 2180688), 532 Alexa Fluor goat anti-mouse (Invitrogen, cat. no. A32727, lot SF251136) and Alexa Fluor 647 goat anti-rabbit (Invitrogen, cat. no. A21244, lot 2179230). Purified m6A-Tracer protein[34] was used at 1:1,000. Embryos were scanned with a 0.3 µm distance between optical sections. Imaging was performed on a Leica TCS SP8 laser scanning confocal microscope with a ×63 oil-immersion objective. Images were processed using Fiji. Image quantification is described in the Supplementary Methods.

Viability assay

The number of embryos that reached the blastocyst after Cbx7–Lap2β or Lap2β injection was assessed at embryonic day 3.5. The starting number of embryos was $n = 67$ for Cbx7–Lap2β and $n = 65$ for Lap2β-injected embryos.

Processing of scDamID and scDam&T-seq data

Data generated using the DamID and scDam&T-seq protocols were largely processed with the workflow and scripts described in ref. 33 (see also www.github.com/KindLab/scDamAndTools). The procedure is described in the Supplementary Methods.

Processing of published data

The accession numbers of all public datasets used are given in Supplementary Table 3 and processing of the data is described in the Supplementary Methods.

Single-cell DamID analyses

Single-cell DamID UMAP. UMAPs based on the single-cell DamID readout in Fig. 1b and Extended Data Fig. 3c were generated by performing a principal component analysis (PCA) on the data and selected the top principal components (PCs) based on the explained variance ratio (PC1–10). These PCs were used as an input to compute the UMAP. In the case of Extended Data Fig. 3c, the maternal and paternal readouts of all samples were treated as separate samples. Consequently, each cell

appears twice in the UMAP: once with the maternal readout and once with the paternal readout.

Cell-to-cell LAD similarity. Cell-to-cell LAD similarity was computed based on the binary contact data of all autosomal chromosomes. To minimize the influence of differential sparsity and noise between LMNB1 datasets, we downsampled all samples being compared with a common threshold and binned data at 1 Mb resolution. These thresholds were: 40,000 total unique GATC sequences (GATCs) (Fig. 1d) and 10,000 allele-specific GATCs (Fig. 5e). For comparison between alleles of the same sample (Fig. 1f), no downsampling was performed because depth-related artifacts are identical for the two alleles. We used Yule's Q as a metric of similarity between cells: $\frac{N_{00}N_{11}-N_{01}N_{10}}{N_{00}N_{11}+N_{01}N_{10}}$, where N_{11} is the number of genomic bins in which both samples had a contact, N_{00} the number of bins in which neither sample had a contact, and N_{01} and N_{10} the number of bins in which one sample had a contact and the other did not.

Cell-to-cell similarity comparison between Dam constructs. Different Dam constructs result in data with vastly different distributions, sparsity and noise levels that will impact the similarity score (Yule's Q), for which downsampling cannot correct. To mitigate the influence of these factors on the similarity score for different Dam constructs, we devised a control for each condition that simulated the expected Yule's Q scores based on technical variability alone. For this, we combined the data of each condition per batch (that is, per sequencing library) and subsequently downsampled the data to generate mock single-cell samples with a number of unique GATCs equal to the actual single-cell data. We subsequently normalized and binarized the simulated single-cell data in a manner identical to the original data. The simulated dataset should thus represent samples that display the same level of technical variability as the original sample, without showing any true biological variation. Finally, we normalized the similarity score of each pair of cells by subtracting their score in the simulated dataset.

LAD coordination. To quantify the coordinated association of genomic bins with the NL, we computed the Pearson correlation between all pairs of genomic bins, as previously described[19]. To control for the influence of technical factors (for example, depth and CF distributions), we compared the observed correlations with those observed when using shuffled binary contact tables. This shuffling was performed in such a way that both marginals (the CF of each 100 kb bin and the total number of contacts in each cell) remained intact, using a published algorithm[35]. For each condition, we performed 1,000 randomizations of the binary contact matrix and computed the bin–bin correlations of the resulting matrices. The observed mean and standard deviation of the correlation matrices were then used to standardize the true bin–bin correlation matrix. The standardized LAD coordination values were compared with normalized Hi-C interaction frequencies (Extended Data Fig. 6i) by correlating their values up to a distance of 50 Mb. The average LAD coordination over pairs of PADs (Extended Data Fig. 6j) was based on code from Coolpup.py[36].

Clustering of genomic bins. Datasets used for genomic bin clustering (100 kb) were based on LMNB1 data of hybrid zygote, 2-cell and 8-cell embryos, LMNB1 data of mESC, H3K27me3 ChIP-seq data of hybrid PN5 zygote, late 2-cell and 8-cell embryos, and H3K27me3 ChIP-seq data of mESC (H3K27me3 data from ref. 13, GSE76687). Allele-separated data were used for all samples, except H3K27me3 mESC. CF values were used for DamID data, $\log_{10}$-transformed reads per kilobase per million (RPKM) values were used for ChIP-seq data. Only data for autosomal chromosomes were included. Genomic bins were further filtered based on the criteria described in the 'Filtering DamID data' section of the Supplementary Methods. Finally, bins were removed if they overlapped >10% with a 'High Signal Region' or >80% with a 'Low Mappability Region', as defined in the ENCODE mm10 blacklist. For the autosomal chromosomes, this left ~88.2% of the genomic bins to be included in the clustering.

Before clustering, values were standardized, clipped to a range of −2.5 to 2.5, and PCA was performed to remove redundancy in the data. The top PCs were selected based on the explained variance ratio (PC1–5), which collectively accounted for 84.5% of variance in the data. These PCs were subsequently used to compute UMAPs representing the genomic bins, as well as for k-means clustering of all bins. For the k-means clustering, six clusters were chosen. Decreasing the number of clusters resulted in the merging of distinct clusters, whereas increasing the number resulted in two or more clusters with very similar behaviors.

Definition of H3K27me3 categories and intrinsic NL affinity categories. For the analyses presented in Fig. 5 and Extended Data Fig. 7, different categories of H3K27me3 enrichment and NL affinity were defined. For H3K27me3 levels, maternal and paternal genomes were considered separately. Genomic bins (100 kb) were divided into H3K27me3 low (RPKM < 0.2), mid (0.2 ≤ RPKM < 0.8) and high (RPKM ≥ 0.8) (Extended Data Fig. 7c). Intrinsic NL affinity was defined based on A/T content (fraction of A/T bases in 100 kb bins) and thresholds were chosen by comparison with zygote CF values (Extended Data Fig. 7a): low (A/T content < 0.56), mid (0.56 ≤ A/T content < 0.61) and high (A/T content ≥ 0.61) (Extended Data Fig. 7b).

Single-cell transcription analyses

Single-cell CEL-seq2 UMAP. To generate the transcriptional UMAP (Fig. 1c), single-cell transcript tables were processed in R (v. 4.1.2) using Seurat (v. 4.1.0)[37]. Only samples passing transcription and DamID thresholds were included; only scDam&T-seq LMNB1 samples of embryos from homozygous crosses and the mESC samples were used. Genes with counts observed in fewer than 10 cells were excluded and data was normalized using the 'NormalizeData' and 'ScaleData' commands. The UMAP was then generated using the 'FindVariableFeatures', 'RunPCA' and 'RunUMAP' commands.

Cbx7–Lap2β versus Lap2β differential expression. Differential expression between Lap2β and Cbx7–Lap2β conditions was tested for transcriptional data derived from the Dam–LMNB1 scDam&T-seq experiment in hybrid 2-cell embryos, and the whole-embryo CEL-seq2 data from embryos collected at the end of the viability experiment. Data were processed using Seurat's 'NormalizeData' and 'ScaleData'. Differentially expressed genes between were identified using the 'FindMarkers' command. Only genes with an adjusted $P < 0.05$ were considered as differentially expressed. No differentially expressed genes were detected.

Transcription of genes in cells with versus without lamina association. To determine the effect of lamina association on the expression of a gene, we determined for each gene the group of cells in which the 100 kb genomic bin containing the gene transcription start site was in contact with the lamina ('contact') and the group of cells in which it was not ('free'). This was done separately per embryonic stage. The transcript counts of the gene and the total transcript counts were then combined for the two groups, and the expression value (as log(RPM + 10) was determined for each group. Genes were excluded from the analysis if either the contact or free group contained fewer than 10 cells; if the gene was expressed in fewer than 10 cells across both groups; if the gene was located on chromosome X or chromosome Y; or if the gene was annotated as a maternal mRNA transcript by Park et al.[38]. In the case of allele-specific data, genes were also excluded if their transcription start sites fell within a genomic bin that did not show sufficient allele separation (see section 'Filtering of DamID data'). The correlation in gene expression values between contact and free states was computed using Spearman's correlation.

Reporting summary
Further information on research design is available in the Nature Portfolio Reporting Summary linked to this article.

Data availability
All genomic and transcriptomic data generated in this study have been deposited at the Gene Expression Omnibus under accession number GSE218598.

Code availability
All custom code generated as part of this study have been deposited at https://github.com/KindLab/LADs-in-Preimplantation-Development (https://doi.org/10.5281/zenodo.12938262)[39].

References

33. Markodimitraki, C. M. et al. Simultaneous quantification of protein–DNA interactions and transcriptomes in single cells with scDam&T-seq. *Nat. Protoc.* **15**, 1922–1953 (2020).
34. van Schaik, T., Manzo, S. G. & van Steensel, B. Genome-wide mapping and microscopy visualization of protein–DNA interactions by pA-DamID. *Methods Mol. Biol.* **2458**, 215–229 (2022).
35. Strona, G., Nappo, D., Boccacci, F., Fattorini, S. & San-Miguel-Ayanz, J. A fast and unbiased procedure to randomize ecological binary matrices with fixed row and column totals. *Nat. Commun.* **5**, 4114 (2014).
36. Flyamer, I. M., Illingworth, R. S. & Bickmore, W. A. Coolpup.py: versatile pile-up analysis of Hi-C data. *Bioinformatics* **36**, 2980–2985 (2020).
37. Hao, Y. et al. Integrated analysis of multimodal single-cell data. *Cell* **184**, 3573–3587.e29 (2021).
38. Park, S. J. et al. Inferring the choreography of parental genomes during fertilization from ultralarge-scale whole-transcriptome analysis. *Genes Dev.* **27**, 2736–2748 (2013).
39. Franka, J. R. KindLab/LADs-in-Preimplantation-Development: initial release. *Zenodo* https://doi.org/10.5281/zenodo.12938262 (2024).
40. Payne, A. C. et al. In situ genome sequencing resolves DNA sequence and structure in intact biological samples. *Science* **371**, eaay3446 (2021).

Acknowledgements
We thank all the members of the Kind laboratory for their comments throughout the project and their critical reading of the manuscript. We thank E. A. Ozonov for advice on data analysis and G. Fanourgakis for collection of additional *Eed* mKO embryos. This work was supported by an European Research Council (ERC) Starting Grant EpiID (ERC Stg EpiID-678423) and ERC Consolidator Grant FateID (ERC CoG-101002885) and a Dutch Research Council Domain Science (NWO-ENW) Vidi grant (grant no. 161.339). The Oncode Institute is partially funded by the KWF Dutch Cancer Society. I.G. was supported by an EMBO Long-Term Fellowship (grant no. ALTF1214-2016), the Swiss National Science Fund (grant no. P400PB_186758) and an NWO-ENW Veni grant (VI.Veni.202.073). The lab of A.H.M.F.P. has received funding from the Novartis Research Foundation and the ERC under the European Union's Horizon 2020 research and innovation program (grant agreement ERC-AdG 695288 - Totipotency). In addition, we would like to thank the Hubrecht Sorting Facility as well as the Utrecht Sequencing Facility, subsidized by the University Medical Center Utrecht and the Netherlands X-omics Initiative (NWO project no. 184.034.019).

Author contributions
I.G., F.J.R. and J. Kind designed the study. F.J.R. performed all data analysis with input from I.G. All embryo and scDam&T-seq experiments were performed by I.G. unless otherwise stated, with assistance from C.K.-V., F.C.G. and R.E.v.B. Zygote injections were performed by C.K.-V. and J. Korving except when using the *Eed* mKO mouse line. Y.K.K. performed the embryo experiments for the *Eed* mKO line and the corresponding control with supervision from A.H.M.F.P. S.J.A.L. and E.B. generated the mESC line expressing Dam–LMNB1 and performed the mESC scDam&T-seq experiment. I.G. and F.J.R. wrote the manuscript with editing by J. Kind. All authors reviewed and edited the manuscript.

Competing interests
The authors declare no competing interests.

Additional information
Extended data is available for this paper at https://doi.org/10.1038/s41588-024-01902-8.

Supplementary information The online version contains supplementary material available at https://doi.org/10.1038/s41588-024-01902-8.

Correspondence and requests for materials should be addressed to Isabel Guerreiro or Jop Kind.

Peer review information *Nature Genetics* thanks the anonymous reviewer(s) for their contribution to the peer review of this work. Peer reviewer reports are available.

https://doi.org/10.1038/s41588-024-01902-8

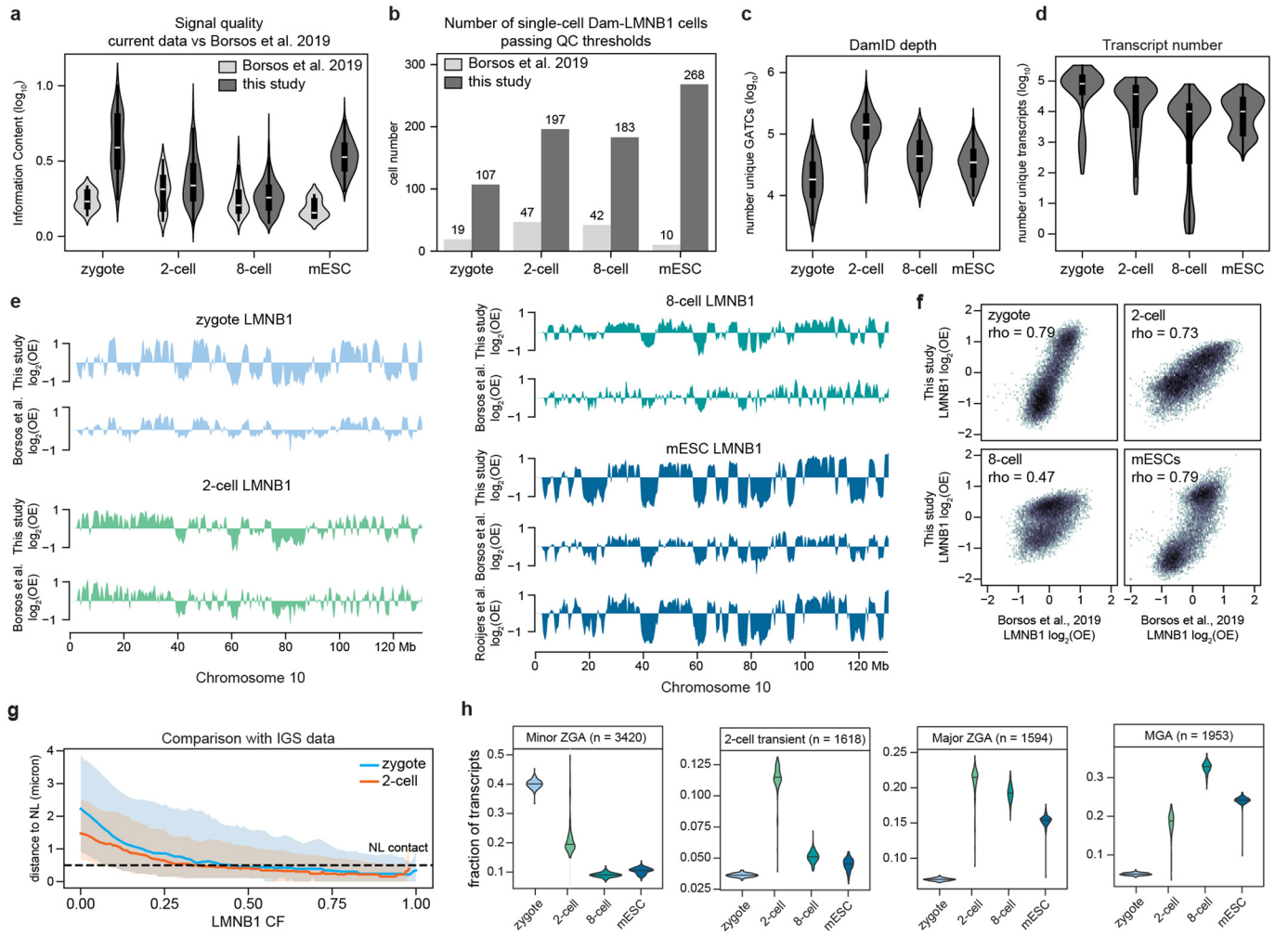

Extended Data Fig. 1 | Validation of single-cell LAD data during preimplantation stages. a, Information content (signal quality) plotted for samples from the present study and Borsos et al.[1]. Borsos: zygote, n = 19 cells; 2-cell, n = 47 cells; 8-cell, n = 42 cells; mESC, n = 10 cells. This study: zygote, n = 107 cells; 2-cell, n = 201 cells; 8-cell, n = 215 cells; mESC, n = 268 cells. Cells passing the DamID depth threshold are included. **b**, Comparison of cell numbers that pass all DamID quality thresholds for the present study and Borsos et al.[1]. **c**, Distribution of unique number of GATCs per stage. Borsos: zygote, n = 19 cells; 2-cell, n = 47 cells; 8-cell, n = 42 cells; mESC, n = 10 cells. This study: zygote, n = 107 cells; 2-cell, n = 197 cells; 8-cell, n = 183 cells; mESC, n = 268 cells. Cells passing all DamID quality thresholds are included. **d**, Distribution of unique transcripts per stage. Zygote, n = 246 cells; 2-cell, n = 210 cells; 8-cell, n = 501 cells; mESC, n = 374 cells. All cells are included. **e**, Combined single-cell profiles normalized to mappability (log_2OE) of this work compared to previous studies[1,18] over the entire chromosome 10. **f**, Comparison of single-cell averages from our study and Borsos et al.[1] using mappability normalized values (log_2(OE)) in 100-kb bins (n = 23,751). Correlations were computed using Spearman's rank-order correlation (zygote, rho = 0.79, p < 1e-100; 2-cell, rho = 0.73, p < 1e-100; 8-cell, rho = 0.47, p < 1e-100; mESC, rho = 0.79, p < 1e-100). **g**, Comparison of zygote and 2-cell LMNB1 CF and distance to the NL as reported in Payne et al.[40] by in situ genome sequencing (IGS). The line shows the median distance of all fragments with a certain CF value, the shaded area shows the inter-quartile range. The dashed line indicates the distance threshold used to designate a genomic region as contacting the NL by Payne et al.[40] **h**, Distribution of the fraction of total transcripts that correspond to different gene categories per stage, as defined in Park et al.[38]. Minor ZGA, n = 3,420 genes; 2-cell transient, n = 1,618 genes; Major ZGA, n = 1,594 genes; MGA, n = 1,953 genes. ZGA, zygotic genome activation; MGA, mid-preimplantation gene activation. Black line indicates median values. Boxplots included in (**a**), (**c**), and (**d**) indicate median values (white line), inter-quartile range (IQR, black box) and the range of all data points within 1.5 times the IQR (whiskers).

https://doi.org/10.1038/s41588-024-01902-8

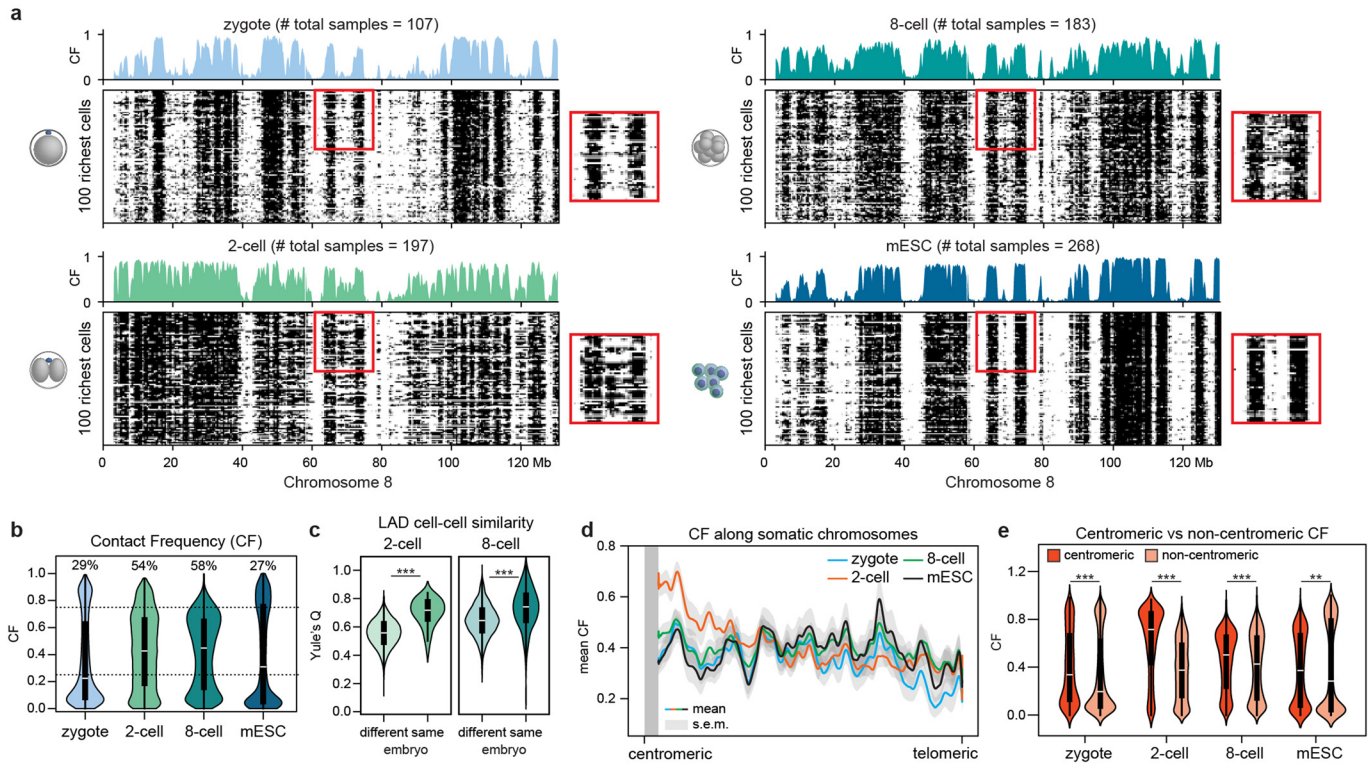

Extended Data Fig. 2 | Analysis of cell-to-cell LAD variability in preimplantation stages and mESCs. a, Heatmaps show single-cell binarized profiles of 100 example cells that passed quality thresholds along the entire chromosome 8 (left panel) ordered by unique number of unique GATCs (DamID depth) for each stage. Tracks on top of the heatmaps show contact frequency (CF) profiles. On the right side of each heatmap is a magnification of the region highlighted with a red rectangle. **b**, Distribution of CF values in 100-kb bins per stage (n = 23,751 bins). On top, percentages of bins between 0.25 and 0.75 CF values, which are indicative of cell-to-cell variability, are shown. **c**, Violin plot showing cell-to-cell similarity using Yule's Q on cell pairs originating from the same embryo or from a different embryo at the 2-cell stage (left) and at the 8-cell stage (right). Two-sided Mann-Whitney U test was performed (2-cell different embryo, n = 16,944; 2-cell same embryo, n = 76, p = 8.0e-28; 8-cell different embryo, n = 4,744, 8-cell same embryo: n = 206, p = 1.2e-24). **d**, Smoothed mean (1000-Mb Gaussian kernel) of LMNB1 CF values along the length of all autosomal chromosomes scaled to the same size per stage. Shaded areas around the lines indicate the standard error of the mean. **e**, Violin plot depicting CF values in the first 30 Mb (n = 4,984 100-kb bins) versus the remainder of the chromosome (n = 18,767 100-kb bins) for the zygote (p = 9.3e-57), 2-cell (p < 1e-100), 8-cell (p = 6.2e-22) stages and mESCs (p = 1.3e-3). Statistical significance was tested using a two-sided Mann-Whitney U test. Boxplots included in (**b**), (**c**), and (**e**) indicate median values (white line), inter-quartile range (IQR, black box) and the range of all data points within 1.5 times the IQR (whiskers).

https://doi.org/10.1038/s41588-024-01902-8

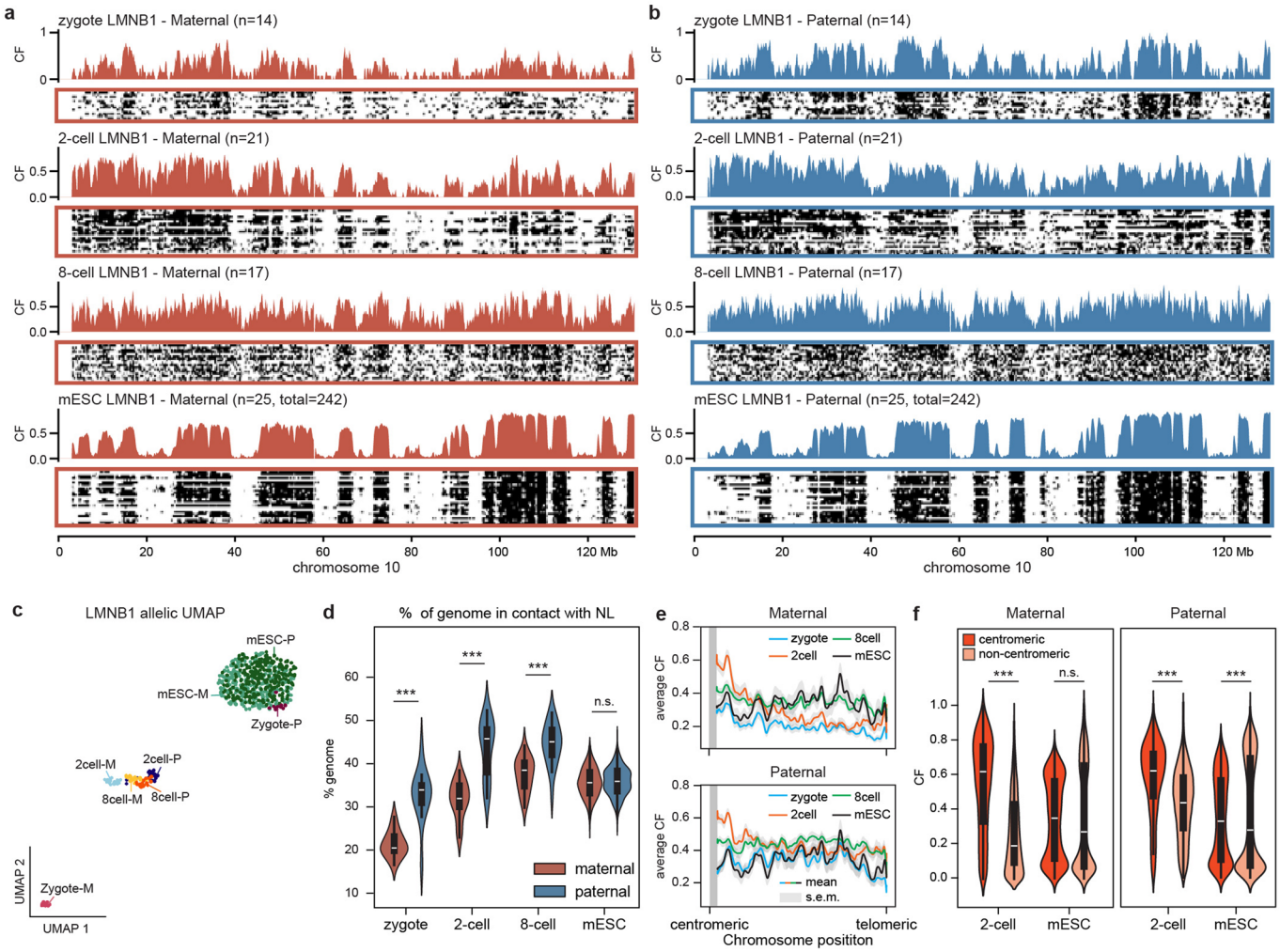

Extended Data Fig. 3 | Characterization of single-cell LAD profiles split by parental allele. a-b, Contact Frequency (CF) tracks and heatmap of binarized single-cell LAD profiles separated into maternal (**a**) and paternal (**b**) allele for the zygote, 2-cell, 8-cell and mESCs along the entire chromosome 10. Heatmaps are ordered by unique number of GATCs (DamID depth). A subset of the total number of mESC is shown. **c**, UMAP based on allelic Dam-LMNB1 single-cell readout. **d**, Percentage of the genome that is in contact with the NL per allele and per stage. Two-sided Wilcoxon rank-sum test was performed (zygote, n = 14, p = 9.4e-5; 2-cell, n = 26, p = 1.83e-7; 8-cell, n = 21, p = 2.5e-5; mESC, n = 268, p-value = 0.36). **e**, Smoothed mean (1000-Mb Gaussian kernel) of LMNB1 CF values along the length of all autosomal chromosomes scaled to the same size per stage and split by allele (maternal - top and paternal – bottom). Shaded areas around the lines indicate the standard error of the mean. **f**, Violin plot depicting CF values separated by allele in the first 30 Mb (n = 4,865 100-kb bins) versus the remaining of the chromosome (n = 18,330 100-kb bins) for 2-cell embryos and mESCs. Two-sided Mann-Whitney U test was performed (2-cell maternal, p < 1e-100; 2-cell paternal, p = 1e-100; mESC maternal, p = 0.60; mESC paternal, p = 2.3e-4). Boxplots included in (**d**) and (**f**) indicate median values (white line), inter-quartile range (IQR, black box) and the range of all data points within 1.5 times the IQR (whiskers).

https://doi.org/10.1038/s41588-024-01902-8

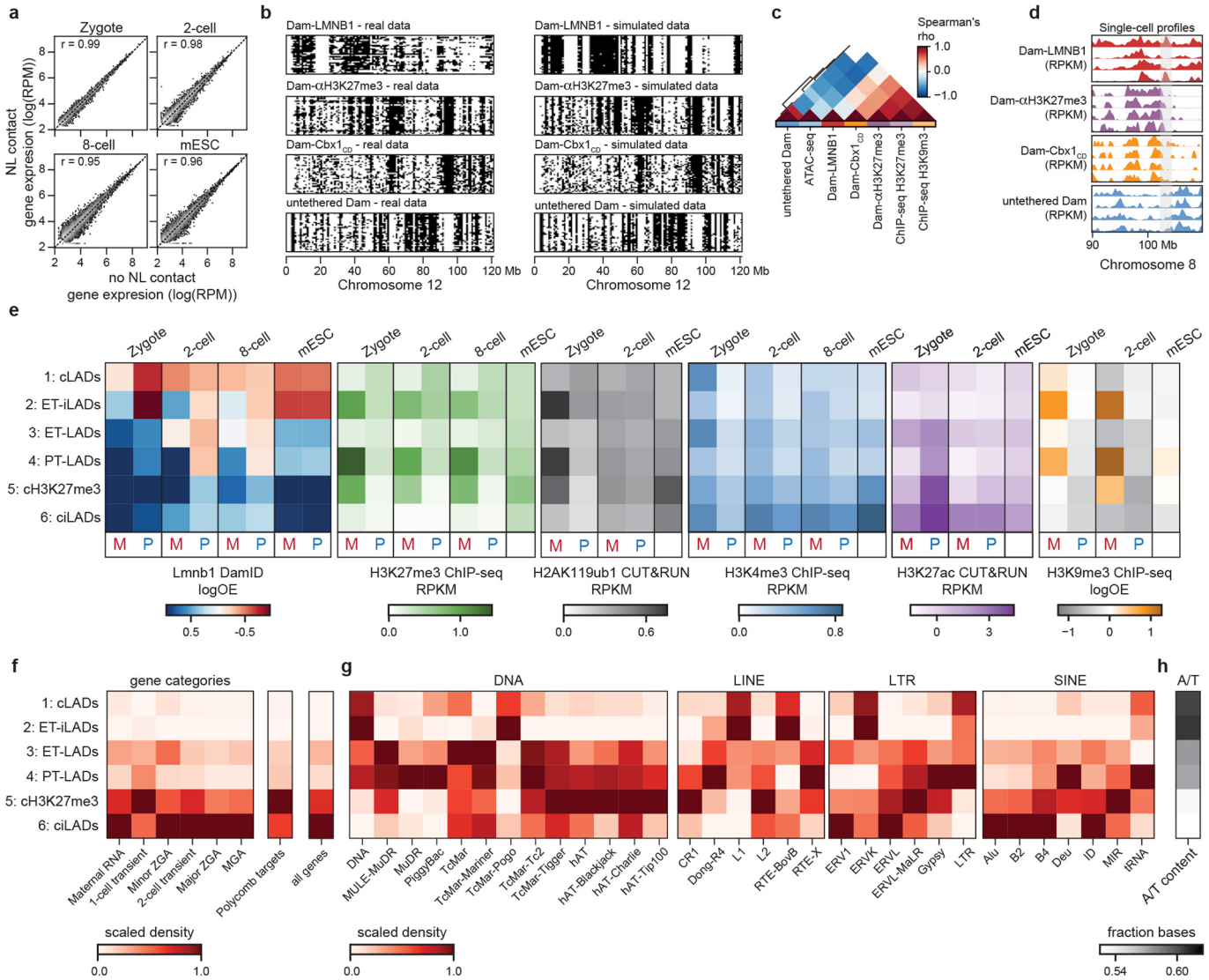

Extended Data Fig. 4 | Validation and analysis of single-cell epigenetic marks at the 2-cell stage. a, Gene expression comparison between cells in which the gene contacts the NL and cells for which the same gene does not contact the NL. Correlation was computed using Pearson's correlation (zyogte, $p < 1e\text{-}100$, $n = 9{,}415$ genes; 2-cell, $p < 1e\text{-}100$, $n = 9{,}143$ genes; 8-cell, $p < 1e\text{-}100$, $n = 8.879$ genes; mESC, $p < 1e\text{-}100$, $n = 9{,}119$ genes). Dashed lines show diagonal. **b**, Left: Heatmap of binarized single-cell profiles for Dam-LMNB1, Dam-αH3K27me3, Dam-Cbx1$_{CD}$ across the entire chromosome 12 ordered by decreasing unique number of GATCs. 30 cells are plotted per construct. Right: Heatmaps showing simulated single-cell samples. This data is used to correct cell-to-cell similarity calculations for construct-specific noise and sparsity levels. **c**, Correlation heatmap relating DamID (present study) and corresponding publicly available ChIP-seq measurements[13] at the 2-cell stage. **d**, Example tracks of four example single cells per construct over a selected region in chromosome 8. A region with high LMNB1 variability is highlighted in grey. **e**, Heatmap with LMNB1 $\log_2$(OE), H3K27me3 RPKM[13] H2Aub RPKM[10], H3K4me3 RPKM[12], H3K27ac RPKM[23] and H3K9me3 $\log_2$(OE)[11], average values per genomic cluster defined in Fig. 2e. **f**, Heatmap showing scaled gene density of different categories described in Park et al. (2013)[50], Polycomb targets[53] and coding genes for each cluster. Scaling is done per column to accommodate the vastly different numbers per column. **g**, Heatmap showing scaled repeat density of each genomic cluster split by repeat family and (**h**) A/T content as fraction of bases per bin. Scaling is done per column to accommodate the vastly different numbers per column.

https://doi.org/10.1038/s41588-024-01902-8

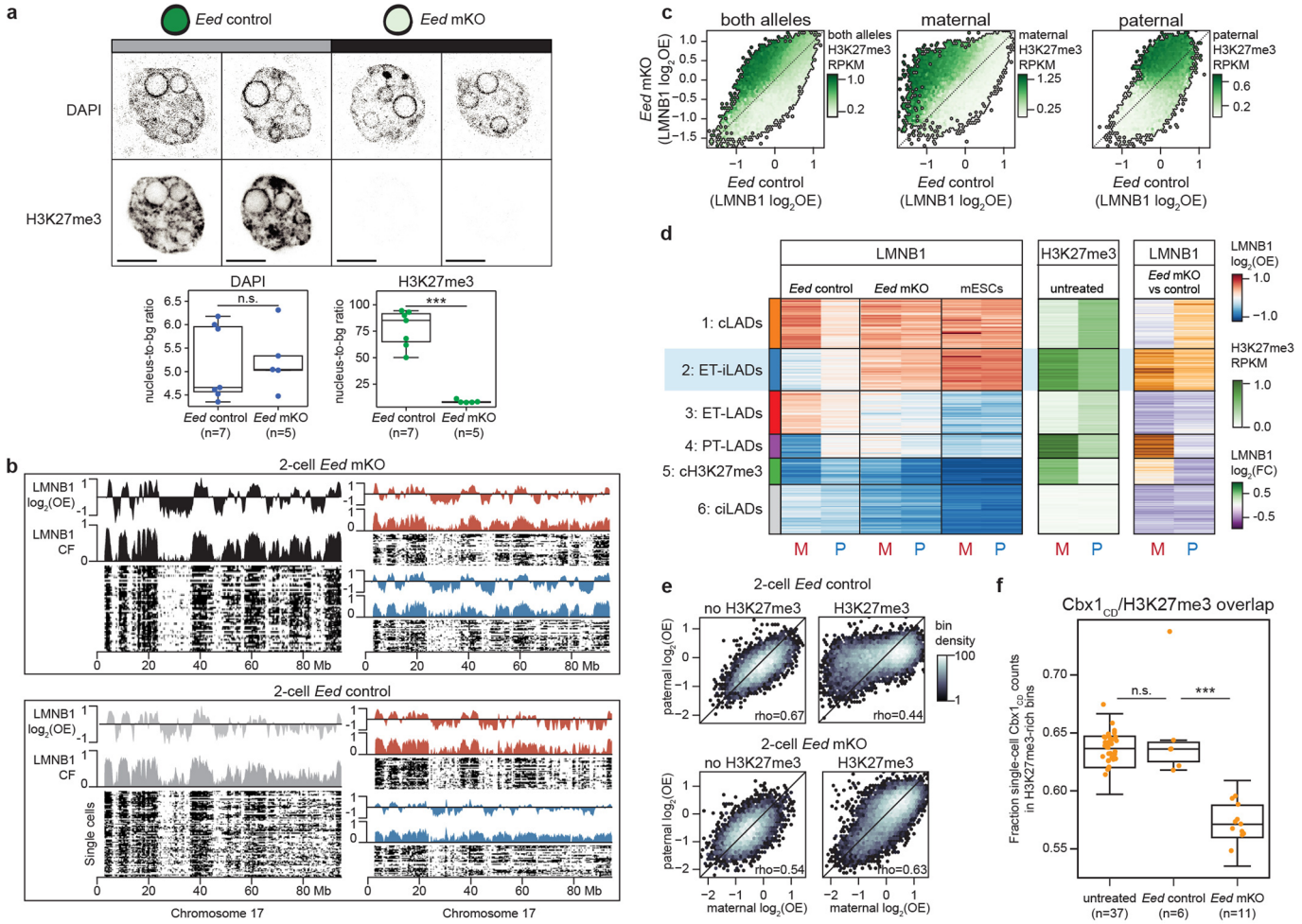

Extended Data Fig. 5 | Effect of *Eed* mKO on nuclear lamina association at the 2-cell stage. a, Top: DAPI and immunostaining of H3K27me3 in 2-cell *Eed* mKO or *Eed* control embryos (scale bar = 10µm). Bottom: Quantification of the nucleus-to-background ratio. Two-sided Welch's T-test was performed to test significance (DAPI, p = 0.89; H3K27me3, p = 4.0e-5; *Eed* control, n = 7 nuclei; *Eed* mKO, n = 5 nuclei). Data is from one biological replicate. **b**, Single-cell heatmaps of binarized LMNB1 profiles of 2-cell *Eed* mKO (top) and control (bottom) embryos with corresponding CF and log_2(OE) values per condition along chromosome 17 of both alleles (left) or separated alleles (right). **c**, Comparison of LMNB1 values in 100-kb bins between *Eed* mKO and control conditions for both alleles (left), or maternal and paternal alleles separately (right). The color refers to average combined or allele-specific H3K27me3 values of 2-cell WT embryos[13]. **d**, Heatmap showing *Eed* mKO and control LMNB1 log_2(OE) values per genomic bin at the 2-cell stage, as well as mESC. 2-cell H3K27me3 (ref. 13) and differential LAD values between the two conditions for each of the genomic clusters depicted in Fig. 2e. **e**, Comparison of maternal and paternal LMNB1 log_2(OE) in 100-kb genomic bins containing H3K27me3 (right) or not (left) in either the control 2-cell condition (top) or in the *Eed* mKO (bottom). Color scale refers to density of genomic bins. Correlations were computed using Spearman's rank-order correlation. *Eed* control & no H3K27me3, rho = 0.67, p < 1e-100, n = 6,662 bins. *Eed* control & H3K27me3, rho = 0.44, p < 1e-100, n = 14,053 bins; *Eed* mKO & no H3K27me3, rho = 0.54, p < 1e-100, n = 6,662 bins; *Eed* mKO & H3K27me3, rho = 0.63, p < 1e-100, n = 14,053 bins. **f**, Boxplot showing fraction of Dam-$Cbx1_{CD}$ counts overlap with H3K27me3-rich (RPKM > 0.2) bins in untreated (n = 37), *Eed* control (n = 6) and *Eed* mKO (n = 11) conditions. Two-sided Mann-Whitney U test was performed to test significance (*Eed* control vs untreated, p = 0.88; *Eed* control vs *Eed* mKO, p = 1.6e-4). Boxplots indicate median values (white line), inter-quartile range (IQR, black box) and the range of all data points within 1.5 times the IQR (whiskers).

https://doi.org/10.1038/s41588-024-01902-8

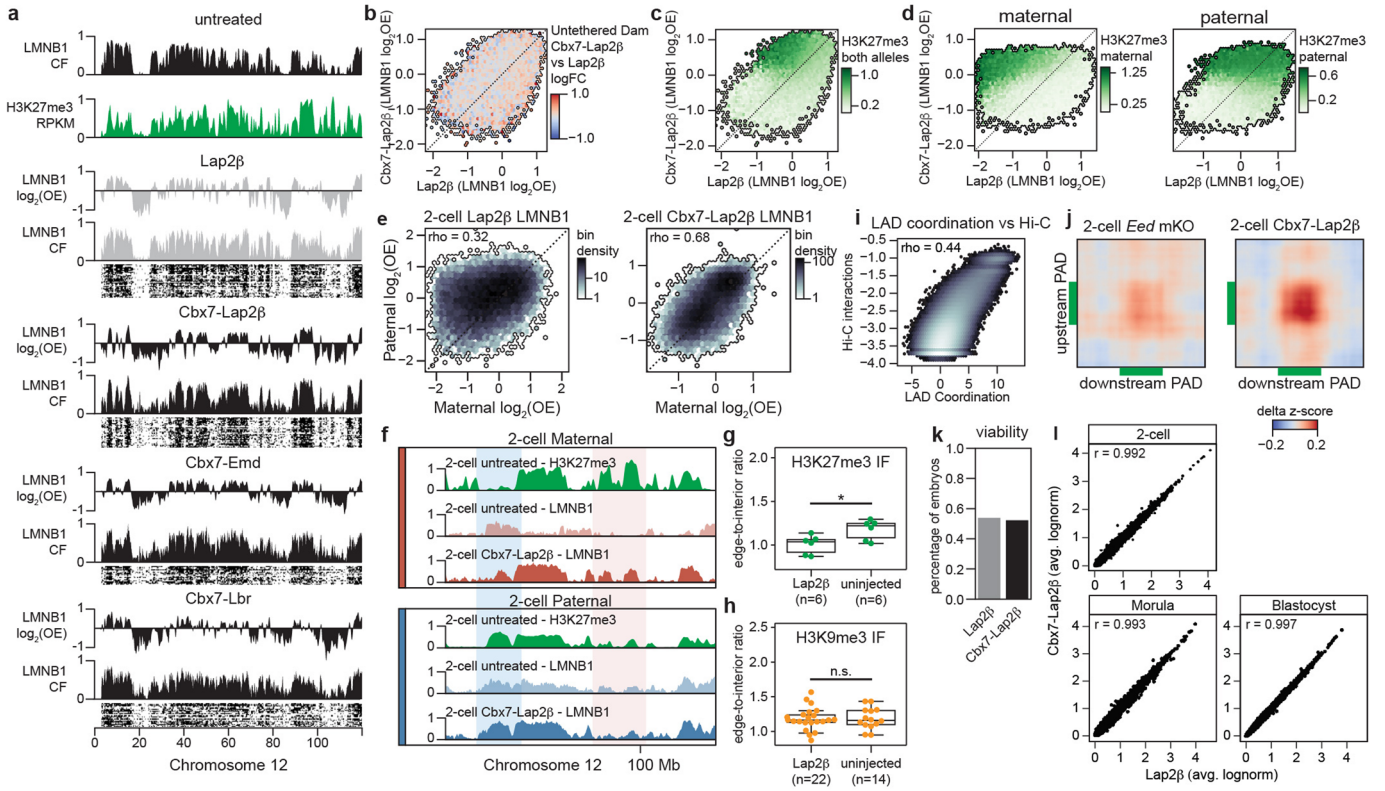

Extended Data Fig. 6 | Effect of H3K27me3-tethering to the NL nuclear lamina. a, Single-cell heatmaps of binarized LMNB1 profiles of *Lap2β*, *Cbx7-Lap2β*, *Cbx7-Emd*, *Cbx7-Lbr* 2-cell embryos with corresponding CF and log_2(OE) values along chromosome 12. On top, 2-cell LMNB1 CF and H3K27me3 (ref. 13) of untreated embryos are show. **b**, Comparison of LMNB1 values in 100-kb bins for the Cbx7-Lap2β and the Lap2β conditions. The color indicates the average log_2(FC) of untethered Dam between Cbx7-Lap2β and Lap2β embryos. **c-d**, Comparison of LMNB1 values in the *Cbx7-Lap2β* and *Lap2β*-injected hybrid embryos for both alleles (**c**) or maternal and paternal alleles separately (**d**). The color scale indicates the average allele-specific H3K27me3 values of 2-cell WT embryos[13]. **e**, Comparison of paternal and maternal LMNB1 CF in Lap2β (left, rho = 0.32, p < 1e-100, n = 21,710 bins) and Cbx7-Lap2β conditions (right, rho = 0.68, p < 1e-100, n = 21,710 bins). Correlations were computed using Spearman's rank-order correlation. **f**, Example genomic region with maternal (top) and paternal (bottom) LMNB1 CF for Cbx7-Lap2β and Lap2β conditions and 2-cell WT H3K27me3. Dashed boxes highlight examples of allelic LAD asymmetry in the Cbx7-Lap2β condition: paternal-specific LADs in blue and maternal-specific LADs in red. **g-h**, Quantification of the radial (1 µm) enrichment of H3K27me3 (**g**) and H3K9me3 (**h**) relative to the rest of the nucleus. Significance was computed using Welch's two-sided t-test (H3K27me3, p = 0.024; H3K9me3, p = 0.96). H3K27me3: Lap2β, n = 6; uninjected, n = 6. H3K9me3: Lap2β, n = 22; uninjected, n = 14. Data is from one biological replicate. Boxplots indicate median values (white line), inter-quartile range (IQR, black box) and the range within 1.5 times the IQR (whiskers). **i**, Correlation between LAD coordination metric and Hi-C interaction values up to 50 Mb distance (rho = 0.44, p < 1e-100, n = 5,311,617 100-kb bin pairs). **j**, Average LAD coordination between PAD pairs up to 20 Mb distance. **k**, Fraction of embryos reaching the blastocyst stage (E3.5) in Cbx7-Lap2β and Lap2β conditions (Cbx7-Lap2β, n = 67; Lap2β, n = 65). Data is from one biological replicate. **l**, Gene expression comparison between Cbx7-Lap2β and Lap2β embryos at 2-cell, morula and blastocyst stages. No significant differentially expressed genes were detected. Pearson's correlation was computed (2-cell, p < 2.2e-16, n = 14,862 genes; morula, p < 2.2e-16, n = 15259 genes; blastocyst, p < 2.2e-16, n = 15,259 genes). Correlations in (**e**) and (**g**) were computed using Spearman's rank-order correlation.

https://doi.org/10.1038/s41588-024-01902-8

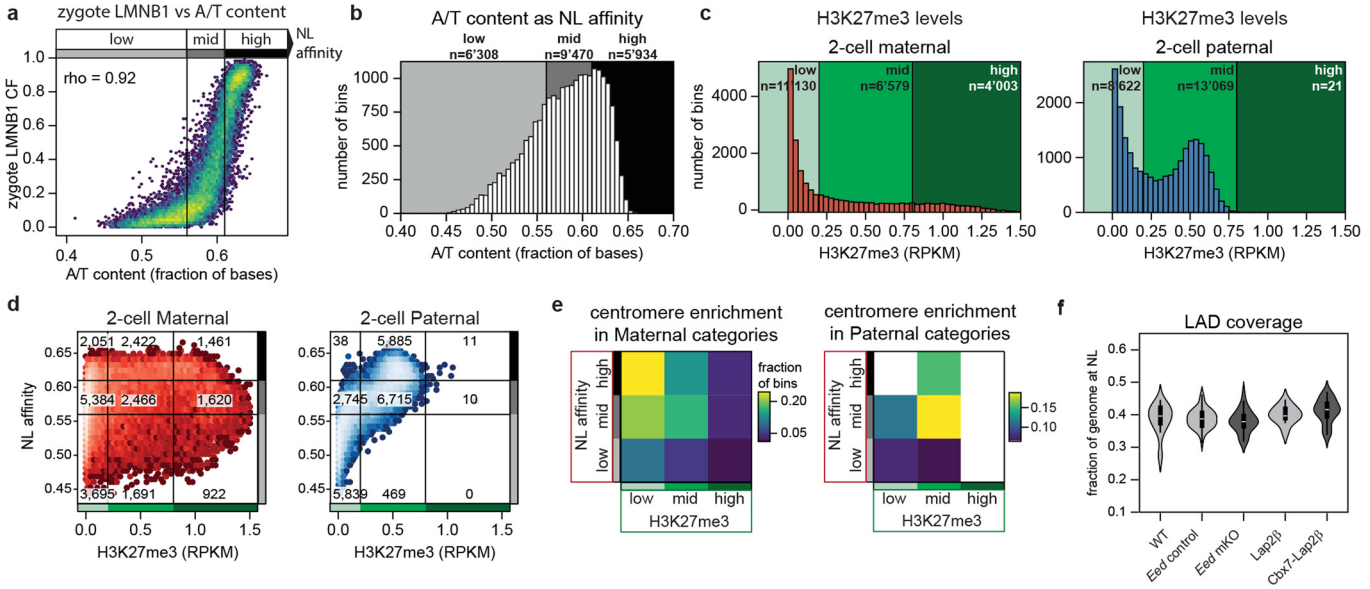

Extended Data Fig. 7 | A model based on NL affinity and H3K27me3 to explain atypical LADs of the early embryo. a, Comparison between zygote LMNB1 CF and A/T content in 100-kb bins (n = 21,708). Thresholds used for low, mid and high intrinsic NL affinity are depicted. Correlation is computed with Spearman's rank-sum correlation (rho = 0.92, p < 1e-100). **b**, Histogram showing the distribution of A/T content in 100-kb bins of the mouse genome. Low, mid and high intrinsic NL affinity categories are highlighted by using increasingly darker colors of the gray scale. **c**, Histogram showing 2-cell WT H3K27me3 RPKM distribution in the maternal (left) and paternal (right) alleles. Low, mid and high H3K27me3 categories are highlighted by using increasingly darker colors of green. **d**, Genome-wide comparison of NL affinity (A/T content) and maternal (red, left) or paternal (blue, right) H3K27me3 RPKM values in 100-kb bins. Categories defined by thresholds set in (**b-c**) are shown with the corresponding color. Number of genomic bins per category is displayed. **e**, Heatmap showing the fraction of bins in each category that is <20 Mb from the centromere. **f**, Distributions of the total fraction of the genome in association with the NL across cells per condition. The total fraction is computed as the average fraction of the maternal and paternal alleles. WT, n = 21 cells; *Eed* control, n = 51 cells; *Eed* mKO, n = 31 cells; Lap2β, n = 10 cells; Cbx7-Lap2β, n = 39 cells. Boxplots indicate median values (white line), inter-quartile range (IQR, black box) and the range of all data points within 1.5 times the IQR (whiskers).

nature portfolio

Corresponding author(s): Jop Kind

Last updated by author(s): 2024/07/27

Reporting Summary

Nature Portfolio wishes to improve the reproducibility of the work that we publish. This form provides structure for consistency and transparency in reporting. For further information on Nature Portfolio policies, see our Editorial Policies and the Editorial Policy Checklist.

Statistics

For all statistical analyses, confirm that the following items are present in the figure legend, table legend, main text, or Methods section.

n/a	Confirmed
☐	☒ The exact sample size (*n*) for each experimental group/condition, given as a discrete number and unit of measurement
☐	☒ A statement on whether measurements were taken from distinct samples or whether the same sample was measured repeatedly
☐	☒ The statistical test(s) used AND whether they are one- or two-sided *Only common tests should be described solely by name; describe more complex techniques in the Methods section.*
☒	☐ A description of all covariates tested
☐	☒ A description of any assumptions or corrections, such as tests of normality and adjustment for multiple comparisons
☐	☒ A full description of the statistical parameters including central tendency (e.g. means) or other basic estimates (e.g. regression coefficient) AND variation (e.g. standard deviation) or associated estimates of uncertainty (e.g. confidence intervals)
☐	☒ For null hypothesis testing, the test statistic (e.g. *F*, *t*, *r*) with confidence intervals, effect sizes, degrees of freedom and *P* value noted *Give P values as exact values whenever suitable.*
☒	☐ For Bayesian analysis, information on the choice of priors and Markov chain Monte Carlo settings
☒	☐ For hierarchical and complex designs, identification of the appropriate level for tests and full reporting of outcomes
☐	☒ Estimates of effect sizes (e.g. Cohen's *d*, Pearson's *r*), indicating how they were calculated

Our web collection on statistics for biologists contains articles on many of the points above.

Software and code

Policy information about availability of computer code

Data collection	Bowtie2 (2.3.3.1) Hisat2 (2.1.0) samtools (1.17) scDamAndTools (1.0)
Data analysis	Python (3.6) scDamAndTools (1.0) deepTools (3.3.0) Hi-C Pro (2.11.4) HiCExplorer (2.2.1.1) Cooler (0.8.11) CoolTools (0.5.1) Numpy (1.20.3) Pandas (2.0.3) scikit-image (0.19.2) scikit-learn (1.3.1) scipy (1.7.1) seaborn (0.13.0) Custom codes, available at github.com/KindLab/LADs-in-Preimplantation-Development (DOI:10.5281/zenodo.12938262).

For manuscripts utilizing custom algorithms or software that are central to the research but not yet described in published literature, software must be made available to editors and reviewers. We strongly encourage code deposition in a community repository (e.g. GitHub). See the Nature Portfolio guidelines for submitting code & software for further information.

Data

Policy information about availability of data

All manuscripts must include a data availability statement. This statement should provide the following information, where applicable:

- Accession codes, unique identifiers, or web links for publicly available datasets
- A description of any restrictions on data availability
- For clinical datasets or third party data, please ensure that the statement adheres to our policy

All data analysis steps are thoroughly described in the manuscript. In addition, custom code used in the data analysis for this manuscript can be accessed at github.com/KindLab/LADs-in-Preimplantation-Development (DOI:10.5281/zenodo.12938262). All sequencing data has been deposited in the GEO database under accession GSE218598: https://www.ncbi.nlm.nih.gov/geo/query/acc.cgi?acc=GSE218598. Accession codes of publicly available datasets used in this study are listed in Extended Data Table 3.

Human research participants

Policy information about studies involving human research participants and Sex and Gender in Research.

Reporting on sex and gender	This study did not include human research participants.
Population characteristics	This study did not include human research participants.
Recruitment	This study did not include human research participants.
Ethics oversight	This study did not include human research participants.

Note that full information on the approval of the study protocol must also be provided in the manuscript.

Field-specific reporting

Please select the one below that is the best fit for your research. If you are not sure, read the appropriate sections before making your selection.

☒ Life sciences ☐ Behavioural & social sciences ☐ Ecological, evolutionary & environmental sciences

For a reference copy of the document with all sections, see nature.com/documents/nr-reporting-summary-flat.pdf

Life sciences study design

All studies must disclose on these points even when the disclosure is negative.

Sample size	Since we did not set out to measure any particular effect, no sample size calculations could be performed. As is the nature of (explorative) single-cell studies, increasing sample numbers will result in charting cellular heterogeneity at higher resolution. The use of live animals severely limited the sample numbers that could be obtained. For our initial dataset (homozygous WT zygote, 2-cell and 8-cell embryos injected with Dam-LMNB1 mRNA), we aimed for at least 100 cells per condition to be able to determine the CF of each genomic locus at <=1% increments. For additional experiments, including different conditions and treatments, we found that lower sample numbers were acceptable, since the observed heterogeneity was lower.
Data exclusions	For some analysis sex chromosomes were left out of the analysis to avoid biases. This exclusion is clearly stated in the methods, main text or figure legends. In addition, some cells didn't pass quality control thresholds relating to read depth, signal quality, etc. These filtering steps are well documented in the manuscript as well.
Replication	For single-cell sequencing experiments, we consider individual embryos as technical replicates (TR), since each embryo presents a distinct mRNA injection event. Note that 2-cell and 8-cell embryos give rise to multiple cells in the dataset. Embryo collections that were performed at different days and were processed separately are considered biological replicates (BR). After filtering single-cells on data quality (DamID thresholds), our study included the following replicates: • Dam-LMNB1 zygote embryos homozygous WT: 4 BR – 8/48/27/24 TR • Dam-LMNB1 2-cell embryos homozygous WT: 6 BR – 6/35/24/18/28/1 TR • Dam-LMNB1 8-cell embryos homozygous WT: 4 BR – 2/8/12/18 TR • Dam-LMNB1 zygote embryos F1xCAST WT: 2 BR – 12/2 TR • Dam-LMNB1 2-cell embryos F1xCAST WT: 2 BR – 10/6 TR • Dam-LMNB1 8-cell embryos F1xCAST WT: 1 BR – 21 TR • Dam-LMNB1 2-cell embryos BL6xJF1 Eed control: 2 BR – 23/37 TR • Dam-LMNB1 2-cell embryos BL6xJF1 Eed mKO: 2 BR – 3/31 TR • Dam-LMNB1 2-cell embryos homozygous Cbx7(CD)-Emd: 1 BR – 10 TR • Dam-LMNB1 2-cell embryos homozygous Cbx7(CD)-Lap2b: 1 BR – 18 TR • Dam-LMNB1 2-cell embryos homozygous Cbx7(CD)-Lbr: 1 BR – 13 TR

• Dam-LMNB1 2-cell embryos homozygous Lap2b: 2 BR – 2/22 TR
• Dam-LMNB1 2-cell embryos F1xCAST Cbx7(CD)-Lap2b: 1 BR – 21 TR
• Dam-LMNB1 2-cell embryos F1xCAST Lap2b: 1 BR – 6 TR
• Dam-LMNB1 mESC BL6xCAST WT: 1 BR – 1 TR (268 cells)
• Dam 2-cell embryos homozygous WT: 2 BR – 23/27 TR
• Dam 2-cell embryos homozygous Cbx7(CD)-Lap2b: 1 BR – 17 TR
• Dam 2-cell embryos homozygous Lap2b: 1 BR – 9 TR
• Dam-aH3K27me3 2-cell embryos homozygous WT: 2 BR – 3/12 TR
• Dam-Cbx1(CD) 2-cell embryos homozygous WT: 1 BR – 22 TR
• Dam-Cbx1(CD) 2-cell embryos BL6xJF1 Eed control: 1 BR – 6 TR
• Dam-Cbx1(CD) 2-cell embryos BL6xJF1 Eed mKO: 1 BR – 11 TR

For the viability experiment:
• Cbx7-Lap2b: 1 BR (67 embryos)
• Lap2b: 1 BR (65 embryos)

For the microscopy experiments:
• H3K27me3 IF on 2-cell embryos Cbx7(CD)-Lap2b (injected): 1 BR – 9 TR
• H3K27me3 IF on 2-cell embryos Cbx7(CD)-Lap2b (uninjected): 1 BR – 3 TR
• H3K27me3 IF on 2-cell embryos Lap2b (injected): 1 BR – 3 TR
• H3K27me3 IF on 2-cell embryos Lap2b (uninjected): 1 BR – 3 TR
• H3K9me3 IF on 2-cell embryos Cbx7(CD)-Lap2b (injected): 1 BR – 17 TR
• H3K9me3 IF on 2-cell embryos Cbx7(CD)-Lap2b (uninjected): 1 BR – 7 TR
• H3K9me3 IF on 2-cell embryos Lap2b (injected): 1 BR – 11 TR
• H3K9me3 IF on 2-cell embryos Lap2b (uninjected): 1 BR – 8 TR
• H3K27me3 IF on 2-cell embryos Eed control: 1 BR – 4 TR
• H3K27me3 IF on 2-cell embryos Eed mKO: 1 BR – 3 TR
• H3K9me3 IF on 2-cell embryos Eed control: 1 BR – 15 TR
• H3K9me3 IF on 2-cell embryos Eed mKO: 1 BR – 11 TR

Due to the manual nature of mRNA injection into embryos, not all injections were successful. For sequencing experiments, unsuccessful injections were automatically filtered out during QC due to the absence of signal or complete saturation of signal.

Randomization

For experiments in WT embryos, one Dam construct was collected per injection day and one developmental stage was collected. This was due to the relatively low number of available embryos and challenges in sample processing when handling different time points. However, frequently these cells were later processed together with cells injected with other constructs/strain/stage. For perturbations, embryos were collected in parallel (for Eed mKO and Eed control) or allocated randomly to experimental groups (Cbx7(CD)-Lap2b vs Lap2b).

Blinding

Blinding was not used in this study: Data was extensively compared to previous studies for the purposes of validation and there was stronger correlation among single cells undergoing the same condition compared to the correlation with single cells of a different stage/construct. Blinding was not used because the aim of experiments was to compare conditions, not make unbiased predictions based on sample data.

Reporting for specific materials, systems and methods

We require information from authors about some types of materials, experimental systems and methods used in many studies. Here, indicate whether each material, system or method listed is relevant to your study. If you are not sure if a list item applies to your research, read the appropriate section before selecting a response.

Materials & experimental systems

n/a	Involved in the study
☐	☒ Antibodies
☐	☒ Eukaryotic cell lines
☒	☐ Palaeontology and archaeology
☐	☒ Animals and other organisms
☒	☐ Clinical data
☒	☐ Dual use research of concern

Methods

n/a	Involved in the study
☒	☐ ChIP-seq
☒	☐ Flow cytometry
☒	☐ MRI-based neuroimaging

Antibodies

Antibodies used

Primary antibodies used were:
rabbit anti-H3K27me3 (Cell Signalling Technology, C36B11, lot 19) at 1:200
rabbit anti-H3K9me3 (abcam, ab8898, lot GR3281994-1) at 1:300
chicken anti-GFP (Aves, GFP-1020, lot GFP697986) at 1:1000
mouse anti-HA (Cell Signaling Technologies, C29F4, lot 9) at 1:500
mouse anti-V5 (Invitrogen R960-25, 2106326) at 1:5000
rabbit anti-LaminB1 (Abcam, ab16048, GR3398321-1) at 1:500 for IF and 1:5000 for Western blot
rabbit anti-HA antibody (Abcam, ab9110, unknown lot number) at 1:5000

Secondary antibodies were all used at 1:500:

	Alexa Fluor 488 Goat anti-Chicken (Invitrogen, A11039, lot 2180688) Alexa Fluor 532 Goat anti-Mouse (Invitrogen, A32727, lot SF251136) Alexa Fluor 647 Goat anti-Rabbit (Invitrogen, A21244, lot 2179230)
Validation	All antibodies are commercially available and have been verified for specificity as stated in the corresponding specification sheets. Antibodies were selected based on their compatibility with immunostainings as indicated by the supplier as well previous experience and publications by the lab. Antibodies are widely used in our lab for immunostaininngs and genomic assays and show similar stainings to published datasets. Anti-GFP, anti-H3K27me3, anti-H3K9me3, anti-V5 and corresponding secondary antibody stainings have been previously published by our lab in Rang et al, Mol Cell (2022). Anti-LMNB1 has been used in Kind et al, Cell (2013). Anti-HA is stated to be suitable for immunofluorescence by the supplier.

Eukaryotic cell lines

Policy information about cell lines and Sex and Gender in Research

Cell line source(s)	Mouse F1 hybrid Cast/EiJ (paternal) x 129SvJae (maternal) embryonic stem cells (mESCs; a gift from the Joost Gribnau laboratory).
Authentication	The cell line was not authenticated.
Mycoplasma contamination	The cell line tested negative for mycoplasma contamination.
Commonly misidentified lines (See ICLAC register)	No commonly misidentified cell lines were used in this study.

Animals and other research organisms

Policy information about studies involving animals; ARRIVE guidelines recommended for reporting animal research, and Sex and Gender in Research

Laboratory animals	Species: mouse Lines: WT, Eedfl/fl;Gdf9-icre and Eedfl/fl Strains: B6CBAF1/J (WT), CAST/EiJ (WT), C57BL/6J (Eed lines), JF1/MsJ (Eed lines) Age: females < 4 months and males < 12 months Dark/light cycle: lights on at 5:00, lights out at 19:00 Temperature: 20-24C Humidity: 40-65%
Wild animals	The study did not involve wild animals.
Reporting on sex	Sex-based analysis were not performed since this study relates to very early stages of development where embryo gender is not expected to bias the analysis. However, due to differences in sex chromosomes between male and female embryos, only autosomal chromosomes were considered in the analysis.
Field-collected samples	The study did not involve samples collected in the field.
Ethics oversight	All animal experiments were approved by the animal ethics committee of the Royal Netherlands Academy of Arts and Sciences (KNAW) under project license AVD801002016728 with study dossiers HI173301 and HI213301 and project license AVD80100202215998 with study dossiers HIKin159982301 and HiKin159982201.

Note that full information on the approval of the study protocol must also be provided in the manuscript.